Topological Mixed Valence Model for Twisted Bilayer Graphene

Liam L. H. Lau[1,*] and Piers Coleman[1,2]

[1]*Center for Materials Theory, Department of Physics and Astronomy, Rutgers University, 136 Frelinghuysen Road, Piscataway, New Jersey 08854-8019, USA*

[2]*Department of Physics, Royal Holloway, University of London, Egham, Surrey TW20 0EX, United Kingdom*

(Received 18 July 2024; revised 4 February 2025; accepted 24 March 2025; published 24 April 2025)

Song and Bernevig (SB) have recently proposed a topological heavy-fermion description of the physics of magic angle twisted bilayer graphene (MATBG), involving the hybridization of flat-band electrons with a relativistic conduction sea. Here, we explore the consequences of this model, seeking a synthesis of understanding drawn from heavy-fermion physics and MATBG experiments. Our work identifies a key discrepancy between measured and calculated on-site Coulomb interactions, implicating renormalization effects that are not contained in the current model. With these considerations in mind, we consider a SB model with a single, renormalized on-site interaction between the f electrons, containing a phenomenological heavy-fermion binding potential on the moiré AA sites. This feature allows the simplified model to capture the periodic reset of the chemical potential with filling and the observed stability of local moment behavior. We argue that a two-stage Kondo effect will develop in MATBG as a consequence of the relativistic conduction band: Kondo I occurs at high temperatures, establishing a coherent hybridization at the Γ points and a non-Fermi liquid of incoherent fermions at the moiré K points; at much lower temperatures, Kondo II leads to a Fermi liquid in the flat band. Utilizing an auxiliary-rotor approach, we formulate a mean-field treatment of MATBG that captures this physics, describing the evolution of the normal state across a full range of filling factors. By contrasting the relative timescales of phonons and valence fluctuations in bulk heavy-fermion materials with that of MATBG, we are led to propose a valley-polaron origin to the Coulomb renormalization and the heavy-fermion binding potential identified from experiment. We also discuss the possibility that the two-fluid, non-Fermi liquid physics of the relativistic Kondo lattice is responsible for the strange-metal physics observed in MATBG.

DOI: 10.1103/PhysRevX.15.021028

Subject Areas: Condensed Matter Physics, Strongly Correlated Materials

I. INTRODUCTION

The discovery of magic angle twisted bilayer graphene (MATBG), developing flat bands at "magic angles" [1–6], has opened a new avenue for the exploration of quantum materials. At integral filling, novel spin and valley polarized [7–11] Mott insulators develop, which on doping transform into strange metals [12–20] and superconductors [4,21] that have attracted intense theoretical study [22–49]. It is as if by tuning the gate voltage one can now explore a family of compounds along an entire row of the periodic table. This *"gate-tuned chemistry"* poses a novel challenge to theoretical work.

Various experiments suggest that electrons localized in the moiré hexagons of MATBG resemble quantum dots [50–52], forming localized moments with valley and spin degeneracy near integer filling. This evidence includes the lifting of spin and valley degeneracy observed in Landau fans [53], a field-tunable excess electronic entropy at integer filling [54], and the appearance of upper and lower Hubbard bandlike features in scanning tunneling microscopy measurements [55]. While the Bistritzer-MacDonald [2] model for magic angle graphene provides an accurate description of the plane-wave single-particle physics, the presence of local moments governed by short-range Coulomb interactions underlines the importance of developing a real-space description of the physics while taking the topology of the system into account [22–25,47,56–67].

Various works have suggested a close analogy between MATBG and f-electron heavy-fermion materials [22–25], opening the problem up to the diverse conceptual and computational methodologies developed for these systems. This paper explores the implications of a recent theory by Song and Bernevig (SB) [24,68] which succinctly describes TBG as a topological *heavy-fermion* problem: Rather

*Contact author: liam.lh.lau@physics.rutgers.edu

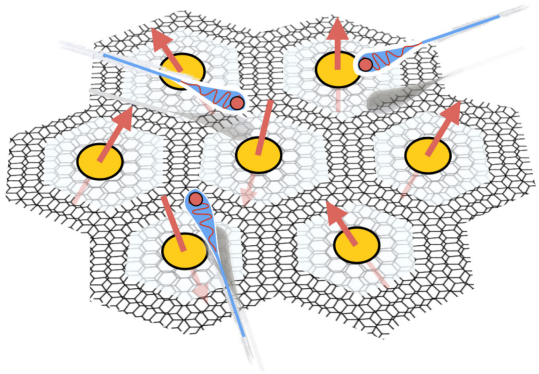

FIG. 1. Hexagonal lattice of exponentially localized Wannier f states (orange) on each moiré AA site submerged in a sea of topological relativistic c electrons (blue).

remarkably, the moiré potential focuses the electron waves into Wannier states that are tightly localized at the center of each moiré hexagon. These localized "heavy fermions" carry spin ($\sigma = \pm 1$), valley ($\eta = \pm 1$), and orbital ($\alpha = \pm 1$) quantum numbers, forming an eightfold degenerate multiplet that becomes mobile through the effects of valence fluctuations into a topological conduction band.

The hybridization of these flat-band ("f") Wannier states with a topological conduction ("c") band captures the essential mirror, time reversal, and particle-hole symmetries of the Bistritzer-MacDonald model (Fig. 1). In particular, the SB model establishes the correct band symmetries at the Γ_M and M_M points of the Brillouin zone, giving rise to a pair of Dirac cones of the same chirality at the K_M points of each valley. The $C_{2z}T$ and particle hole symmetry anomalies responsible for the Dirac cones are reproduced by a quadratic conduction band touching at Γ_M: When hybridization is turned on, this anomaly is injected into the f-electron band (Fig. 2).

Previous studies on the SB model [69–74] have adopted a fixed neutrality assumption, in which the on-site Coulomb interaction takes the form $(U/2)(n_f - 4)^2$ and departures from neutrality are accomplished by varying a uniform chemical potential, while treating all other interactions in a Hartree-Fock approximation. Various approaches have been used to describe the on-site physics, including auxiliary bosons [72], impurity approximations with Wilsonian renormalization group [73], dynamical mean-field theory [23,74], and a slave boson approach [72].

In this paper, we build on these early Kondo lattice models of MATBG, seeking to combine the key features of the SB model with insights drawn from experiment and bulk heavy-fermion physics. In this paper, we focus on the paramagnetic phases of MATBG that develop away from integral filling factors. Highlighted aspects of our work are as follows.

(i) *A discrepancy* identified between the *ab initio* scale of on-site interactions $U_0 \sim 100$ meV in the SB model and the experimentally observed values of $U \sim 30$ meV, pointing to renormalization effects that lie beyond the current model.

(ii) *An f-electron binding potential* of strength $-U\kappa\nu$, introduced phenomenologically to model the periodic reset in chemical potential and the diminished average inverse compressibility $\Delta\mu/\Delta\nu = U(1-\kappa)$.

(iii) *An auxiliary-rotor* mean-field theory [75,76] to describe the alternating patterns of Kondo and valence fluctuations in the paramagnetic phases across all filling factors $\nu \in [-4, 4]$.

(iv) *Two temperature scales*—The Dirac character of the conduction sea in MATBG profoundly affects the Kondo effect, leading to two competing fixed points: a high-temperature scale $T_K^{(1)}$ associated with the formation of the topological band and a considerably lower temperature $T_K^{(2)}$ associated with the development of coherence at the moiré K points.

Key to the heavy-fermion model of MATBG is an understanding of the binding potential that stabilizes

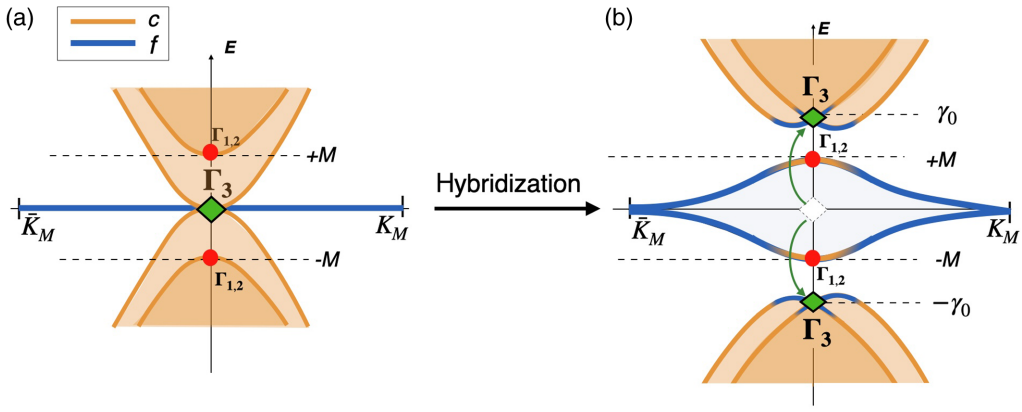

FIG. 2. Schematic illustration of the Song-Bernevig model [24,68], showing (a) the unhybridized flat (f) band (blue) and relativistic conduction band (c) (orange) with quadratic touching Γ_3 symmetry (green diamond) and $\Gamma_{1,2}$ symmetry points (red disk) with an excitation gap M; (b) hybridization causes band inversion between the Γ_3 and $\Gamma_{1,2}$ points, injecting topological conduction states into the flat f band.

localized f states at various integer filling factors ν. The simplest view treats the back gate of MATBG as a capacitor that subjects the conduction sea and f level to a single chemical potential; in this picture, a unit increase in the filling requires the chemical potential to shift by the Coulomb energy—i.e., the coarse-grained inverse compressibility is given by $\Delta\mu/\Delta\nu = U$. Experimentally, however, the chemical potential rises by an amount that is considerably smaller than the observed on-site interaction. For example, STM experiments at the *AA* sites of MATBG observe cascades in the electronic structure associated with an on-site $U \sim 30$ meV (blue read off from the upper and lower Hubbard band position from the *AA* data in Ref. [50] and rounded up from 23 ± 5 meV), yet the coarse-grained inverse compressibility is of the order of $\Delta\mu/\Delta\nu \approx 15$ meV [50].

To shed further light on this physics, it is useful to contrast gate-tuned MATBG with bulk heavy-fermion materials [77–84], where the f states are bound by a nuclear potential whose depth progressively increases with atomic number Z, accommodating the electron repulsion that rises with the filling factor. The slow rise and periodic reset in the chemical potential with filling factor observed in MATBG suggests a corresponding binding mechanism in MATBG: We choose to incorporate the observed physics in a phenomenological Hamiltonian

$$H = H_0 + \frac{U}{2}\sum_{\mathbf{R}}(\hat{\nu}_{f\mathbf{R}} - \kappa\nu)^2, \tag{1}$$

where H_0 is the noninteracting SB Hamiltonian, combined with an on-site Coulomb interaction of strength U among the f electrons centered in the moiré unit cell at $\mathbf{R}$, where $\hat{\nu}_{f\mathbf{R}} = \hat{n}_{f\mathbf{R}} - 4$ is their number operator relative to half filling. This shifts the neutrality point of the Coulomb interaction to $n_f = 4 + \nu$, where $\nu \propto V_g$ is directly proportional to the back-gate voltage.

While we introduce the attractive binding potential $-U\kappa\nu\hat{\nu}_{f\mathbf{R}}$ phenomenologically to explain the partial chemical potential reset seen in experiment [50–52,60], this mechanism appears implicitly in previous DMFT + Hartree studies [47,74] from an *ad hoc* Hartree treatment of the interactions between the dispersive and localized states [24,47,74]. Our work explicitly highlights the vital role of this term in producing the chemical potential resets and provides a new interpretation of this term as an attractive binding potential for localized states. Given the uncertainties in the Hartree approximation, particularly when the on-site interaction is treated at much higher order in DMFT and the c-f hybridization is handled dynamically, we have adopted a phenomenological approach which leaves the microscopic origin of the binding potential to future debate.

There are two salient insights from our approach which we discuss in depth at the end of this paper. First, contrary to heavy-fermion materials, the optical phonon dynamics in twisted bilayer graphene are fast compared to valence fluctuations of the localized f electrons. The phonons modify the "atomic" Hamiltonian for the localized f electrons in MATBG, giving rise to a Holstein model of the form

$$H = \omega_0 b^\dagger b + g(b + b^\dagger) f^\dagger \tau_x f, \tag{2}$$

where $b^\dagger$ creates the optic phonon and the τ_x couples to the valley degree of freedom. Bridging disparate fields, this leads us revive a previously abandoned concept [85,86] from heavy-fermion physics, proposing that the slow valence fluctuations in MATBG are dressed by intervalley phonons, forming intervalley polarons. Such polarons address the disparity between the measured and calculated on-site Coulomb by inducing the necessary renormalizations but also could provide a natural contribution to the emergent heavy-fermion binding potential $-\kappa U$:

$$\kappa U = \frac{g^2}{\omega_0}, \tag{3}$$

where g is the electron-phonon coupling in Eq. (2). This new perspective offers an attractive synthesis of the high-energy electron-phonon physics, notably present in superconducting samples [87], and low-energy strong correlation physics in MATBG.

A second key insight is that the relativistic character of the Kondo lattice in the SB model sets it apart from conventional bulk heavy-fermion physics. In the corresponding single-impurity problem, a linear conduction density of states generates non-Fermi liquid Kondo screening behavior, with a residual entropy [88]. We posit that the topological character of the flat bands protects this physics in the SB Kondo lattice, providing a possible origin for the observed strange-metal phenomena in these materials. We present a demonstration that this framework yields two characteristic energy scales: a high-temperature scale, due to scaling away from an unstable Withoff-Fradkin fixed point [89], corresponding to the onset of topological effects, and a low-temperature scale associated with the emergence of flat-band coherence and scaling toward a conventional heavy Fermi liquid.

We note that while strain effects [90–94] and substrate alignment [95,96], particularly with hexagonal boron nitride (h-BN), have been demonstrated to impact certain MATBG samples, these effects are omitted here. A brief discussion of these effects is included at the end of the paper.

The outline of the paper is as follows. Section II reviews the Song-Bernevig model; in Sec. III, we use a renormalized Anderson model for MATBG to account for the behavior of both the chemical $\mu[\nu]$ and inverse compressibility $d\mu[\nu]/d\nu$ as functions of the filling ν within the moiré atomic limit of the model. Section IV discusses the effects of turning on interactions in MATBG, identifying

the two characteristic scales of the underlying Landau Fermi liquid. Section IV B examines Kondo scaling in MATBG, using the single-impurity limit to gain insight into the lattice physics, arguing that the presence of a "Withoff-Fradkin fixed point" in the weak-coupling physics introduces two characteristic temperature scales in MATBG. In Sec. V, we employ the auxiliary-rotor mean-field approach [75,76] to describe the low-energy physics of our periodic Anderson model for MATBG. The strength of the auxiliary-rotor method is that it is exact in the strong- and weak-coupling limits; hence, we are able to capture the valence fluctuations and Kondo effect in MATBG at all filling factors using a single theory. Section VI describes the results of calculations using the rotor method. Finally, Sec. VII discusses the physics beyond the current model, including the origins of the renormalization of the on-site Coulomb U and the emergent heavy-fermion potential $-U\kappa\nu$, speculating on the implications of our findings for the future understanding of MATBG.

II. SONG-BERNEVIG MODEL

The one-particle Hamiltonian of the SB model,

$$H_0 = H_c + H_{fc} - \mu\hat{N}, \tag{4}$$

hybridizes exponentially localized Wannier f-electron states centered on the moiré AA sites with topological conduction electrons defined by the Hamiltonian

$$H_c = \sum_{\substack{|\mathbf{k}|<\Lambda_c \\ a,a'\eta\sigma}} c^\dagger_{\mathbf{k}a\eta\sigma}\mathcal{H}^{(\eta)}_{aa'}(\mathbf{k})c_{\mathbf{k}a'\eta\sigma}. \tag{5}$$

Here, $c^\dagger_{\mathbf{k}a\eta\sigma}$ creates a conduction electron with orbital, valley, and spin quantum numbers $a \in (1,4)$, $\nu = \pm$, and $\sigma = \pm 1$, respectively. The conduction electron dispersion

$$\mathcal{H}^{(\eta)}(\mathbf{k}) = \begin{pmatrix} & v_\star(\eta k_x\alpha_0 + ik_y\alpha_z) \\ v_\star(\eta k_x\alpha_0 - ik_y\alpha_z) & M\alpha_x \end{pmatrix} \tag{6}$$

describes the momentum-dependent mixing between the four orbitals in each valley η. The off-diagonal terms give rise to an asymptotically linear dispersion with velocity $v_\star$, where the Pauli matrices $\alpha_\mu \equiv (\alpha_0, \vec{\alpha})$ $(\mu = 0, 3)$ act on the two-dimensional blocks. The first two entries of the matrix $(a = 1, 2)$ refer to electrons with Γ_3 symmetry at the Γ_M, point $\mathbf{k} = 0$, while the lower block-diagonal $a = (3, 4)$ describes two orbitals of Γ_1 and Γ_2 symmetry, split by a mass M.

H_c gives rise to four bands with a fourfold spin-valley degeneracy at each $\mathbf{k}$. The low-energy dispersion is quadratic at Γ_M and becomes relativistic $|E| \sim v_\star k$ at energies $|E| \gtrsim M$, with a bandwidth $D \sim v_\star K_\theta$. The single-particle model for TBG in each valley has a symmetry anomaly in the $C_{2z}T$ and particle-hole P symmetries, corresponding to two Dirac cones at the Fermi level with the *same* chirality. Since the local orbitals are topologically trivial, the unhybridized conduction electron band structure carries the symmetry anomaly.

The hybridization between the conduction sea and f electrons at each moiré AA site $\mathbf{R}$ is described by

$$H_{fc} = \gamma_0 \sum_{\mathbf{R}a\eta\sigma} (f^\dagger_{\mathbf{R}a\eta\sigma} c_{\mathbf{R}a\eta\sigma} + \text{H.c.}). \tag{7}$$

Here, $f^\dagger_{\mathbf{R}a\eta}$ creates an f electron with Γ_3 symmetry, orbital character $\alpha = 1, 2$, and valley and spin quantum numbers η and σ, respectively. The total degeneracy of the bare f states is, thus, $2N_f = 8$. $c^\dagger_{\mathbf{R}a\eta}$ creates a c electron in a nonexponentially localized Wannier state centered at $\mathbf{R}$ with the same Γ_3 symmetry, orbital, spin, and valley quantum numbers as the f electron; it is related to the normalizable continuum $c^\dagger_{\mathbf{k}a\eta\sigma}$ states by

$$c_{\mathbf{R}a\eta\sigma} = \frac{1}{\sqrt{N_s}} \sum_{\substack{\mathbf{k},\mathbf{G},a \\ |\mathbf{k}+\mathbf{G}|<\Lambda_c}} e^{i\mathbf{k}\cdot\mathbf{R}} [\phi^{(\eta)}(\mathbf{k}+\mathbf{G}, \gamma_0)]_{a\alpha} c_{\mathbf{k}+\mathbf{G}a\eta\sigma}, \tag{8}$$

where the sum over all momenta has been divided up into a sum over reciprocal lattice vectors $\mathbf{G}$ of the moiré lattice and a sum over momentum $\mathbf{k}$ restricted to the first moiré Brillouin zone. The matrix form factor is

$$\phi^{(\eta)}(\mathbf{k}) = e^{-|\mathbf{k}|^2\lambda^2/2}\Big(-\alpha_0 + a_\star(\eta k_x\alpha_x + k_y\alpha_y),\ 0_{2\times 2}\Big), \tag{9}$$

where $a_\star$ sets the length scale of the hybridization and λ is a damping factor proportional to the real-space spread of the localized f-Wannier states. Remarkably, the focusing effect of interference of the moiré potential produces Wannier states of size $\lambda \sim a_M/5$, about a fifth of the moiré unit cell size a_M. The natural bandwidth of the free theory is given by $D \sim v_\star K_\theta$, but, after hybridization, M becomes the bandwidth of the moiré flat bands, while γ_0 is the energy of the Γ_3 irrep of the higher-energy bands at the Γ_M point. In MATBG, the case where $M = 0$ corresponds to the special *chiral* limit of twisted bilayer graphene, where the hybridized f-c band is *completely* flat [97,98].

Finally, $\hat{N}$ is the total electron count measured relative to neutrality:

$$\hat{N} = \sum_{\substack{|\mathbf{k}|<\Lambda_c \\ a\eta\sigma}} \left(c^\dagger_{\mathbf{k}a\eta\sigma} c_{\mathbf{k}a\eta\sigma} - \frac{1}{2}\right) + \sum_{\mathbf{R}a\eta\sigma} \left(f^\dagger_{\mathbf{R}a\eta\sigma} f_{\mathbf{R}a\eta\sigma} - \frac{1}{2}\right), \tag{10}$$

and μ is the chemical potential.

The approximate scales for the parameters in the SB model are [24,68] $D = v_\star K_\theta \approx 133$ meV, $\gamma_0 = 25$ meV, $M = 3.7$ meV, $v_\star = -4.3$ eV Å, $K_\theta = 0.031$ Å^{-1}, $a_\star = 65$ Å, and $\lambda = 0.225 a_M = 29$ Å for the size of the Wannier states, which gives $\tilde{\lambda} = \lambda K_\theta = 0.90$.

The noninteracting SB model reproduces the band structure of the Bistritzer-MacDonald model, giving rise to a central band of width $2M$, split off by an energy γ_0 from the upper and lower bands as illustrated in Fig. 2. The central band can contain up to eight electrons, and, in the noninteracting model, an applied chemical potential causes the band structure to move rigidly, so that, by changing the chemical potential μ over a range from $-M$ to M, the electron count per moiré unit cell can be tuned from 0 to 8.

We note that the chiral limit [97,98] of the Bistritzer-MacDonald model, corresponding to the limit with no tunneling between graphene layers in the AA-stacked regions in TBG, is reproduced when $a_\star = 0$ [24,68]. The central bands become exactly flat at the chiral limit magic angles [97], corresponding to $M = 0$ in the SB model [24,68].

III. INTERACTIONS

An appeal of the SB picture is that it offers the possibility of a simplified model for the interactions between the highly localized f electrons. Song and Bernevig have provided a detailed calculation of the projection of the Coulomb interaction, screened by the back gate, onto the Fock space of f and c electrons, which reveals a hierarchy of interactions.

In a conventional metal, electron charges are compensated by the static charge of the background ions, but, in MATBG, departures from neutrality are compensated by screening charges in the back gate [24,68]. In MATBG, Gauss's law enforces a strict linear relationship between the electron filling of the flat bands and the gate voltage. For a filling ν, the excess charge on the TBG is $q = eN_M\nu$, where N_M is the number of moiré cells. Gauss's law enforces $q = CV_g$, where C is the capacitance of the back-gate-dielectric-MATBG stack and V_g the gate voltage. Thus, it follows that the filling factor

$$\nu = \frac{q}{eN_M} = \frac{CV_g}{eN_M} = \frac{V_g}{\Delta V_g} \tag{11}$$

is a strict linear function of the gate voltage. In essence then, the gate voltage *is* the filling factor, enforcing a canonical ensemble of definite filling factor ν on the flat bands.

The projected Coulomb interaction, screened by the back gate, contains two major on-site interactions, an f-f Coulomb interaction U_{screen} and an f-c Coulomb repulsion W. The scale of the instantaneous Coulomb interactions is determined by the Coulomb integral for an electron in one of the moiré Wannier states,

$$U_{\text{screen}} = \int_{\mathbf{x},\mathbf{x}'} \rho(\mathbf{x}) V(\mathbf{x}-\mathbf{x}') \rho(\mathbf{x}'), \tag{12}$$

where

$$\rho(\mathbf{x}) = \frac{e^{-x^2/\lambda^2}}{\pi\lambda^2} \tag{13}$$

is normalized electron density in the Wannier state, while

$$V(\mathbf{x}-\mathbf{x}') = \frac{e^2}{4\pi\epsilon\epsilon_0} \sum_n \frac{(-1)^n}{\sqrt{|\mathbf{x}-\mathbf{x}'|^2 + (2dn)^2}} \tag{14}$$

is the Coulomb interaction between electrons, modified by the image charges. Here, d is the distance to the back gate. The summation is $\sum_{n=0,1}$ for a single back gate with a single image charge per electron and $\sum_{n=-\infty}^{\infty}$ for a double back gate, where there are the multiply reflected image charges of alternating sign behind the back gates.

An evaluation of the Coulomb integral (Appendix A) gives

$$U_{\text{screen}} = U_0 F\left[\frac{d}{\lambda}\right], \tag{15}$$

where $F[x]$ is a screening function for the appropriate back gate (see Appendix A) and

$$U_0 = \sqrt{\frac{\pi}{2}} \frac{e^2}{4\pi\epsilon\epsilon_0\lambda} \sim 103 \text{ meV} \tag{16}$$

is the unscreened Coulomb energy, estimated, following SB with $\epsilon = 6.0$ as in-plane dielectric constant for a boron-nitride substrate with $\lambda = 2.9$ nm [99]. Figure 3 shows the dependence of the Coulomb integral on the distance d to the back gate, showing how the thinner the back-gate layer, the more screened the Coulomb interaction. Song and Bernevig assume a distance $\xi = 2d \approx 10$ nm to the image charges in the back gate. With these values, Eq. (15) predicts $U_{\text{screen}} \sim 70$ meV, comparable with the value $U_{\text{SB}} \sim 58$ meV obtained in SB. This on-site interaction substantially exceeds the bandwidth of the flat band, leading to a situation in which the electrons are on the brink of localization into states with integer occupations.

There is, however, an important discrepancy between the *ab initio* Coulomb interaction values calculated by Song and Bernevig and that observed experimentally. The STM experiments which reveal localized states at the AA moiré sites [50] indicate a Coulomb interaction $U \approx 30$ meV (read off from the upper and lower Hubbard band position from the AA data in Ref. [50] and rounded up from 23 ± 5 meV). In fact, the discrepancy with theory is even more substantial when we take into account that the devices on which these measurements were made involve a distance of about $d = 320$ nm (combined thickness of around 40 nm for the h-BN and 285 nm for the SiO_2 [100]) between the semiconductor back gate and the MATBG, for which we would expect the much larger value $U \sim U_0$. There is, thus, a factor of 4 discrepancy between the theoretical value of U and that observed in the STM

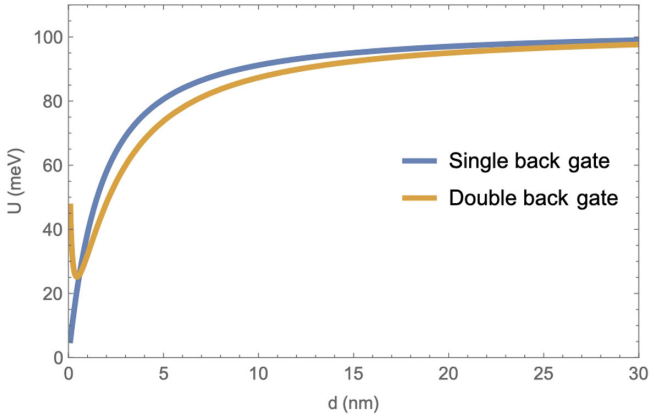

FIG. 3. Showing the dependence of the Coulomb integral as a function of back-gate distance for single and double back-gate devices.

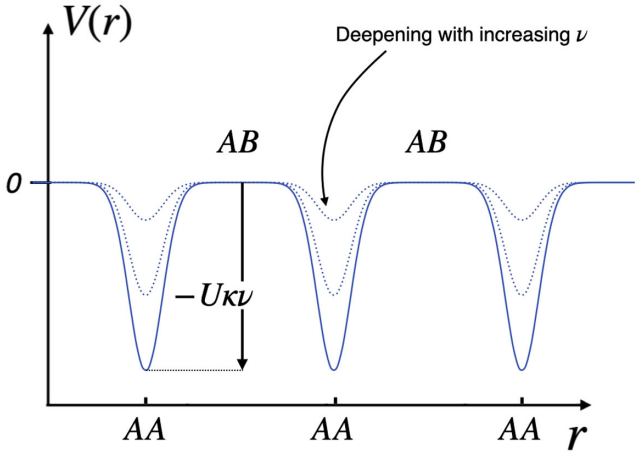

FIG. 4. Emergent heavy-fermion potential on the *AA* sites with a depth proportional to the filling ν. The well becomes progressively deeper with filling, offsetting the Coulomb repulsion between f electrons.

cascade experiments. Indeed, the DMFT study [74] uses interaction scales [24,68] calculated from back-gate distances which are more than an order of magnitude smaller than in the STM cascade experiments [50].

DMFT studies have dealt with this discrepancy either by taking small back-gate distances [74] or by introducing a large, phenomenological dielectric constant $\epsilon = 10$–12 [23,47] for the substrate. This important discrepancy between the measured and *ab initio* Coulomb interactions hints at renormalization effects that lie beyond a static Coulomb interaction.

We note that previous DMFT works [47,74] predict a Hubbard gap smaller than the Hubbard U parameter. However, we believe that the renormalization factor between the gap and U in these references (at best a factor of 2) is insufficient to reconcile the discrepancy between the experimentally measured gap with interaction scale $U = 23 \pm 5$ meV [50] and the much larger interaction scale $U_{\text{screen}} \sim 103$ meV (15) expected from the SB model using the experimental gate distance ($d = 320$ nm) from the Cascades study [50].

One possibility of renormalization effects beyond a static Coulomb interaction is dynamic screening by the lattice, a point we return to in the discussion. Here, though, we assume that these effects can be taken account by a renormalized Anderson model, in which the scale of the interactions is set by experiment.

A. Phenomenological interaction model

Rather than pursuing a comprehensive microscopic approach, we adopt a phenomenological strategy to capture the dependence of the interactions on filling factor. We focus solely on the residual on-site interactions U between the f electrons responsible for the observed Coulomb blockade physics. A second element of our treatment is the introduction of an emergent heavy-fermion potential $-U\kappa\nu$ on the *AA* sites (Fig. 4), which linearly deepens with back-gate voltage $\nu \propto V_g$ The renormalized Anderson model that we work with is the following:

$$H = H_0 + \frac{U}{2}\sum_{\mathbf{R}}(\hat{n}_{f\mathbf{R}} - 4)^2 - U\kappa\nu\sum_{\mathbf{R}}\hat{n}_{f\mathbf{R}} \equiv H_0 + \frac{U}{2}\sum_{\mathbf{R}}(\hat{\nu}_{f\mathbf{R}} - \kappa\nu)^2. \tag{17}$$

The parameter κ controls the emergent heavy-fermion potential on the *AA* sites, and we show in the following subsection that a finite κ is needed to understand the observed reset in the chemical potential μ that occurs as a function of filling factor.

B. Coulomb blockade physics

We begin by considering the unhybridized moiré atomic limit of the renormalized Anderson model (17), given simply by

$$H_A(\mathbf{R}) = \frac{U}{2}(\hat{n}_{f\mathbf{R}} - 4 - \kappa\nu)^2 - \mu\hat{n}_{f\mathbf{R}}. \tag{18}$$

The physics here is similar to a quantum dot. The stability of the quantum dot with $n_f = Q$ f electrons requires that the ionization energies (Appendix B)

$$\Delta E^Q_{\pm} = E_{Q\pm1} - E_Q = \frac{U}{2} \pm [U(1-\kappa)\nu - \mu] \tag{19}$$

are both positive. Here, we set $\nu = Q - 4$. The energies $\pm\Delta E^Q_{\pm}$ describe the offset location for the upper and lower Hubbard peaks in the f-spectral function (Fig. 8). At zero temperature, the local moment with Q f electrons is stable provided that the chemical potential satisfies

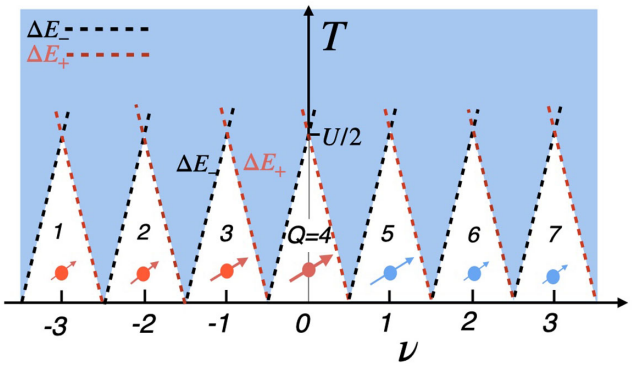

FIG. 5. Sawtooth phase diagram for the moiré atomic limit of MATBG, as a function of filling ν. White regions denote a stable local moment with Q f electrons, bounded by the ionization energies $\Delta E_{\pm}$ for adding or removing one electron.

$$U/2 > |U(1-\kappa)\nu - \mu[\nu]|. \tag{20}$$

To increase the filling factor by one, the chemical potential μ must jump by U at each integer ν. When continuing to fill the moiré atomic model (18) from integer filling $\nu \to \nu + 1$, the extra on-site Coulombic cost U is partially offset by the emergent heavy-fermion potential $\Delta E_f = -U\kappa$. Consequently, the chemical potential must shift $\Delta\mu = U(1-\kappa)$ to fully compensate the Coulombic cost (details in Appendix B).

At a finite temperature, the local moment with Q f electrons is stable provided

$$k_B T < U/2 - |U(1-\kappa)\nu - \mu[\nu]|, \tag{21}$$

which defines the sawtooth phase diagram shown in Fig. 5.

In Fig. 6, we illustrate the chemical potential μ and inverse compressibility $d\mu/d\nu$ as functions of the filling factor ν, depicted in blue, for the moiré atomic limit of the renormalized Anderson model (18) at zero temperature with a finite value of κ.

The presence of a finite hybridization causes the f valence to fluctuate through the virtual emission or absorption of electrons, $f^Q \rightleftharpoons f^{Q-1} + e^-$ and $e^- + f^Q \rightleftharpoons f^{Q+1}$. At energy scales below $U/2$, the physics of the low-energy region are then described by a voltage-tuned "Kondo lattice" [101,102].

The presence of a finite negative gradient in the chemical potential $\mu[\nu]$ in between integer filling factors coupled with evidence of negative inverse compressibility $d\mu/d\nu$ empirically suggests a finite value of κ. From Refs. [50–52,60], we extract phenomenological values of $U \approx 30$ meV and $\kappa \approx 0.8$. We find that the bare Song-Bernevig hybridization γ_0 results in a significant smoothing of the sharp features in the chemical potential $\mu[\nu]$ as a function of filling found in the moiré atomic limit. To preserve the partial resetting behavior, it is crucial to maintain the established hierarchy of energy scales within the heavy-fermion analogy. Specifically, the hybridization between the f electrons and c electrons must undergo renormalization to ensure that the reduced hybridization strength $\gamma_0 \ll U$. We defer the discussion of the possible mechanisms underlying these phenomenological parameters and renormalizations to Sec. VII.

IV. QUALITATIVE CONSIDERATIONS

A. Adiabatic considerations: The heavy Fermi liquid

The noninteracting SB model describes a narrow band of f electrons, with a linear Dirac dispersion of fixed chirality centered the K_M points with a Dirac velocity v_D (see Appendix C):

$$v_D \approx 3\left(\frac{\gamma_K}{D}\right)^2 \frac{M}{D}\left(2(1+a_\star^2 K_\theta^2) + \tilde{\lambda}^2(1-a_\star^2 K_\theta^2)\right) v_\star, \tag{22}$$

where $D = v_* K_\theta$ and $\gamma_K = \gamma_0 e^{-\tilde{\lambda}^2/2}$ is the strength of the hybridization at the K_M point, where $\tilde{\lambda} = K_\theta \lambda$.

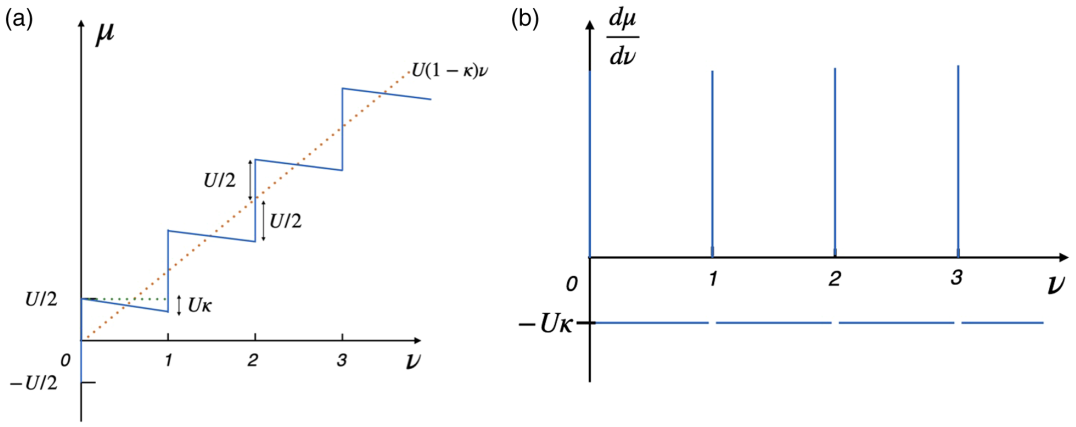

FIG. 6. Sketch in blue of (a) the chemical potential μ and (b) the inverse compressibility $d\mu/d\nu$ as functions of filling factor ν for the moiré atomic limit of the renormalized Anderson model for MATBG at zero temperature for nonzero $0 < \kappa < 1$.

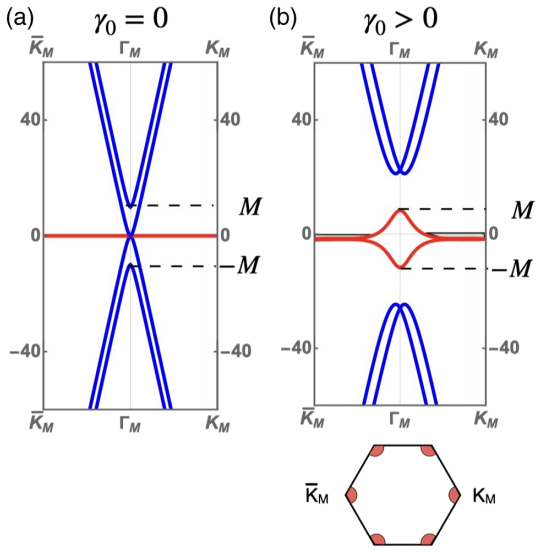

FIG. 7. Schematic contrasting the noninteracting band structure of the SB model at fixed filling for (a) zero and (b) finite hybridization, with zero interaction. The Dirac points sink into the Fermi sea, producing two approximately circular Fermi surfaces of predominantly f character, with fourfold valley spin symmetry, centered at each K_M and $\bar{K}_M$ points.

The approximate bandwidth of this flat band is given by $W = v_D K_\theta$ or

$$W \approx 3\left(\frac{\gamma_K}{D}\right)^2 M\left(2(1 + a_\star^2 K_\theta^2) + \tilde{\lambda}^2(1 - a_\star^2 K_\theta^2)\right). \tag{23}$$

In the third chiral limit (flat limit) [24,68], where $M = 0$, the flat bandwidth identically vanishes. Even in the noninteracting model, there are, in fact, two important energy or temperature scales, a high-temperature scale $T^{(1)} \sim \gamma_0 \sim 25$ meV, below which the excitations are confined within the low-energy flat band, and a much lower scale

$$T^{(2)} \sim \left(\frac{\gamma_0}{D}\right)^2 \left(2(1 + a_\star^2 K_\theta^2) + \tilde{\lambda}^2(1 - a_\star^2 K_\theta^2)\right) M \sim 1.0 \text{ meV}, \tag{24}$$

corresponding to the Fermi temperature of the flat band. This large separation of scales is a key feature of the SB model that we expect to continue when interaction effects are taken into account.

Provided $M > 0$, a Fermi liquid forms, and on doping away from neutrality the Dirac points sink into the Fermi sea, producing two approximately circular Fermi surfaces of predominantly f character (Fig. 7), with fourfold valley spin symmetry, centered at each K_M and $\bar{K}_M$ points, each of area $A_{FS} \sim \pi k_F^2$ area which satisfies Luttinger's sum rule, which we can write as

$$8\frac{A_{FS}}{A_M} = \nu, \tag{25}$$

where A_M is the area of the moiré Brillouin zone. The noninteracting f electrons, thus, form a Dirac sea of relativistic chiral fermions with a bandwidth of approximately $v_D k_F$, occupying a fraction $\nu/8$ of the Brillouin zone. The SB model also predicts that, at the Γ_M point, the energy eigenvalues are $\epsilon_\Gamma = \{\pm M - \mu, \pm\gamma_0 - \mu\}$, where those with energy $\pm M$ are entirely of conduction character, whereas those with energy $\pm\gamma_0 - \mu$ are an equal admixture of f and topological conduction electrons.

Let us consider what happens when interactions are adiabatically introduced at constant filling factor ν to produce a Landau Fermi liquid: This requires that $|M| > 0$. Now the f states renormalize with a quasiparticle weight Z_f characterizing the K_M points of the Brillouin zone. So long as the ground state remains a Fermi liquid, the Fermi surface area remains an adiabatic invariant, which causes the f states to remain pinned close to the Fermi energy, with energies $\epsilon_{\mathbf{k}} = \lambda \pm v_D^*|\mathbf{k} - \mathbf{K_M}|$, where $v^* = Z_f v_D$ is a renormalized Fermi velocity while in $\lambda \sim W^* = Z_f W$ is of the order of the renormalized bandwidth.

The principle energy scales of the SB Anderson lattice can be obtained by considering a corresponding impurity Anderson model, formed from a single moiré f state embedded in a relativistic electron gas. The relativistic character of the conduction sea gives rise to a density of states per moiré per valley per spin, that is linear in energy at high energies. The density of states per spin per valley per orbital in the Γ_3 channel that hybridizes with the f states is

$$\rho_c(E) = \frac{A}{D^2} \times \begin{cases} |E|, & E| > M| \\ \frac{1}{2}(|E| + M), & |E| < M, \end{cases} \tag{26}$$

where $A = 2\pi/(3\sqrt{3}) \approx 1.2$ (see Appendix D). In the presence of a chemical potential, this density of states shifts downward in energy by an amount μ, and now $\rho_c(E, \mu) = \rho_c(E + \mu)$.

If we ignore the effects of interaction, the hybridization width (half width at half maximum) of an isolated noninteracting Anderson impurity using the bare SB hybridization $\gamma_0 = 25$ meV [24,68] is given by

$$\Delta_0[\mu] = \pi\overline{\gamma_0^2(k)}\rho_c(\mu), \tag{27}$$

where $\overline{\gamma_0^2(k)} \approx 2\gamma_0^2$ is the momentum integrated average of the hybridization squared over a circle of radius K_θ (see Appendix E). From Eq. (26), we obtain the noninteracting hybridization width of a single Anderson impurity at neutrality to be

$$\Delta_0(\mu=0)=\frac{\pi A}{2}\frac{\overline{\gamma_0^2(k)}}{D^2}M\approx 0.1M, \tag{28}$$

while, for the full lattice, the bandwidth of the SB model is $W=v_D K_\theta$. From Eq. (22), we obtain

$$W=v_D K_\theta\approx 0.4M. \tag{29}$$

The two quantities $\Delta_0(\mu=0)$ and W are of comparable magnitude at neutrality.

When the interactions are turned on, the f-spectral function splits into an upper and lower Hubbard peak at locations E_+^Q and $-E_-^Q$, with a Kondo resonance in the center as shown in Fig. 8. The upper and lower resonances have a half width of the order of $(2N_f-Q)\Delta_0$ and $Q\Delta_0$, respectively, where $2N_f=8$ for TBG.

B. Withoff-Fradkin scaling and non-Fermi liquid physics

Once the temperature drops below the characteristic energies for valence fluctuations $T\ll \min(\Delta E_\pm^Q)\sim U$, we can integrate out the charge fluctuations to produce a low-energy Kondo lattice description. The resulting low-energy effective Hamiltonian, obtained by performing a Schrieffer-Wolff transformation [102] on Eq. (1),

$$H_K=\sum_{v_\star|\mathbf{k}|<D} c_{\mathbf{k}}^\dagger \mathcal{H}(\mathbf{k})c_{\mathbf{k}}+J_{\rm eff}\sum_{\mathbf{R}BB'} c_{\mathbf{R}B}^\dagger c_{\mathbf{R}B'}S_{BB'}(\mathbf{R}) \tag{30}$$

is a topological Kondo lattice model. Here, $B\equiv(\alpha\eta\sigma)_2\equiv 1,2\ldots 8$ is the SU(8) index written in binary and

$$S_{BB'}(\mathbf{R})=f_{\mathbf{R}B}^\dagger f_{\mathbf{R}B'}-\frac{Q}{2N_f}\delta_{BB'} \tag{31}$$

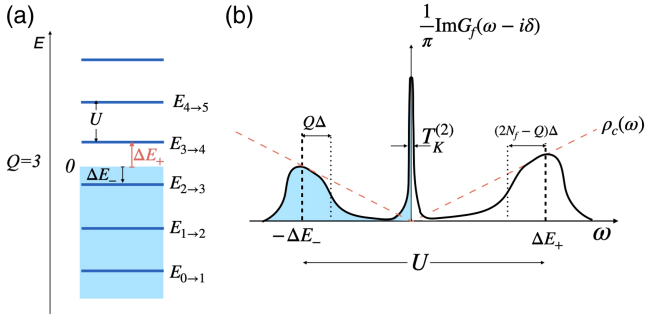

FIG. 8. (a) Energy-level diagram showing the position f-level excitation energies for the case of $Q=3$ f electrons, i.e., $\nu_0=-1$. (b) Spectral function for the f state in an impurity model, showing upper and lower Hubbard resonances and the central Kondo resonance against the background of the linear density of states of the conduction sea.

is the SU (8) spin operator. The operator $c_{\mathbf{R}B}^\dagger\equiv c_{\mathbf{R}(\alpha\eta\sigma)}^\dagger$ defined in Eq. (8) creates a spatially extended Γ_3 conduction electron state, centered (rather than localized) at $\mathbf{R}$ with quantum numbers B. In the Kondo limit $\mu\ll U$, the strength of the effective Kondo interaction

$$J_{\rm eff}=\sum_\pm \frac{(\gamma_0)^2}{\Delta E_{Q\to Q\pm1}}=\frac{4(\gamma_0)^2}{U}F[\delta\nu], \tag{32}$$

where $\delta\nu=\nu-\nu_0$ is the difference between the actual filling ν and the integer moiré atomic filling ν_0 and $F[\delta\nu]=1/[1-(2\delta\nu)^2]$.

To get an idea of the underlying physics of the MATBG Kondo lattice, it is instructive to consider the properties of a corresponding single-impurity model: i.e., consider a thought experiment in which only one moiré AA site is occupied with f electrons. It is particularly instructive to consider the symmetric neutral case where $\nu=0$ and $M=0$ [the third chiral limit (flat limit) of MATBG [24,68]]. In this case, $\rho_c(\omega)\propto|\omega|$. The Kondo coupling $J(\Lambda)$ is governed by the leading-order scaling equation

$$\frac{\partial J}{\partial\ln\Lambda}=-2N_f J(\Lambda)^2\rho_c(\Lambda)+O(J^3), \tag{33}$$

where $N_f=4$ is the valley-spin degeneracy. Rewriting Eq. (33) as a dimensionless coupling constant $g(\Lambda)\equiv J(\Lambda)\rho_c(\Lambda)$, we find that the Kondo coupling constant renormalizes according to the "Withoff-Fradkin" scaling equation [89]:

$$\frac{\partial g}{\partial\ln\Lambda}=g(\Lambda)-2N_f g(\Lambda)^2+O(g^3), \tag{34}$$

where the first term derives from the derivative of the density of states. The competition between the linear and the quadratic terms in this scaling equation gives rise to the unstable Withoff-Fradkin fixed point (Fig. 9), located in this case at $g_c=1/(2N_f)=1/8$. Provided $g>g_c$, a Kondo effect does take place, characterized by a single Kondo temperature $T_K^{(1)}$. However, although g now scales to strong coupling, the fully screened state that develops in a Dirac sea is not a Fermi liquid, forming a Kondo resonance with a singular density of states and a finite residual entanglement entropy [88].

Now, suppose we reintroduce a small finite M (or, alternatively, a departure from neutrality): This will now guarantee a Kondo effect for any value of coupling g. From a scaling perspective, M has the dimensions of energy with leading scaling behavior is $(\partial M/\partial\ln\Lambda)=M$, so that M is a relevant perturbation to the Withoff-Fradkin fixed point, and at scales lower than M, forcing conventional Kondo scaling is reestablished, scaling away to a conventional Fermi liquid strong-coupling fixed point. The schematic scaling phase diagram is shown in Fig. 10.

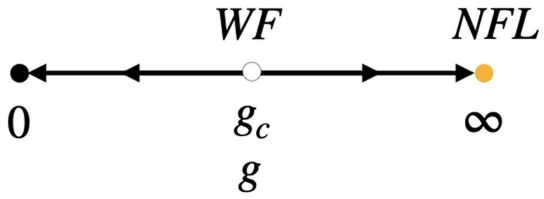

FIG. 9. $M = 0$ scaling diagram for the dimensionless Kondo coupling g, showing the unstable Withoff-Fradkin (WF) fixed point g_c. Flow to weak coupling occurs below WF ($g < g_c$); above WF ($g > g_c$), flow to strong coupling yields a non-Fermi liquid (NFL) fixed point with residual entropy.

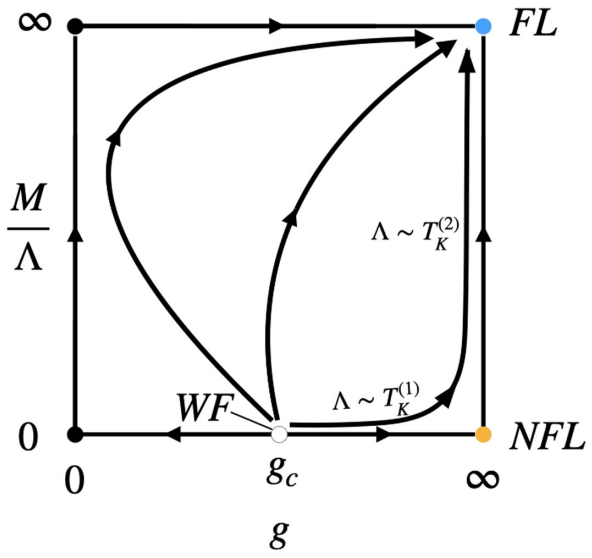

FIG. 10. Schematic scaling trajectories for the (single-ion) Kondo effect within the SB model. Finite M ensures the Kondo effect for all g. For $g > g_c$ and small M, scaling trajectories are initially dominated by the NFL fixed point, corresponding to a high temperature $T_K^{(1)}$. There is then a rapid crossover at $T_K^{(2)}$, when the effect of finite M develops, to a heavy Fermi liquid (FL) fixed point with fully quenched local moments.

In reality, M is finite and we are never precisely at particle-hole symmetry in MATBG; nevertheless, we shall argue that for realistic parameters $g \gtrsim g_c$, so that, over a large temperature range, the physics is dominated by the Kondo effect in a Dirac sea. In particular, for $g > g_c$ and small M, the Kondo scaling trajectories are initially dominated by the non-Fermi liquid fixed point, corresponding to a high Kondo temperature $T_K^{(1)}$. At a much lower temperature $T_K^{(2)}$, the effect of finite M develops, causing the system to lose its residual entanglement entropy at a second, lower-temperature Kondo scale $T_K^{(2)}$.

We can estimate $T_K^{(1)}$ by integrating the scaling equation (34)

$$\int_{g_0}^{1} \frac{dg}{g - 2N_f g^2} = \int_{U/2}^{2\pi T_K^{(1)}} d\ln\Lambda, \tag{35}$$

where $\Lambda_0 \sim U/2$ is the upper cutoff and $2\pi T_K^{(1)}$ is the lower cutoff determined by the Kondo temperature. This then gives

$$T_K^{(1)} = \frac{U}{8\pi(1-g_0)}\left(1 - \frac{g_c}{g_0}\right), \tag{36}$$

where $g_c = 1/2N_f$ and $g_0 = [4\overline{\gamma(k)^2}/U]\rho_c(\Lambda_0)$. For $M = 0$, the third chiral limit (flat limit) [24,68] of MATBG, we expect that

$$T_K^{(1)} \sim \gamma, \tag{37}$$

where γ is the renormalized hybridization gap. We will see that this is confirmed by mean-field theory.

We can also estimate $T_K^{(2)}$ by identifying with the renormalized resonant level width $T_K^{(2)} \sim \Delta$ where the renormalized hybridization $\Delta = 2\pi(\gamma/D)^2 M$ (23), with $\gamma_0 \to \gamma \sim T_K^{(1)}$, which gives

$$T_K^{(2)} \sim \Delta \propto \pi\left(\frac{T_K^{(1)}}{D}\right)^2 M \ll T_K^{(1)} \tag{38}$$

for the Fermi liquid temperature. As in the noninteracting case, there is a very large ratio between the two temperature scales $T_K^{(1,2)}$, and, in the limit $M \to 0$, non-Fermi liquid behavior continues to zero temperature. The scale $T_K^{(2)}$ corresponds to the renormalized Dirac bandwidth of the flat bands. The characteristic size of the screening cloud

$$\xi_K = \frac{v_D}{T_K^{(2)}} \to \infty \tag{39}$$

diverges in the limit $M \to 0$, reflecting the finite entanglement entropy and the critical nature of the Kondo effect at the Withoff-Fradkin fixed point.

Normally, we would expect that a non-Fermi liquid fixed point of a Kondo impurity would not survive in the lattice. However, the crystal symmetries of MATBG guarantee the existence of Dirac cones at the K_M points which become flat when $M = 0$, and, as in the impurity, this fixed point will dominate the physics over a large energy range, guaranteeing the persistence of a two-scale *lattice* Kondo effect in MATBG, allowing us to use the impurity estimates as an order-of-magnitude guide to the corresponding scales in the lattice. We note that the presence of a finite occupancy of the flat bands will then require the Fermi level to be pinned near the Dirac-like dispersion at the moiré K points. (We now show this is the case using a mean-field theory.) In conclusion, we expect that a similar ratio between $T_K^{(1)}$ and $T_K^{(2)}$ will persist in the Kondo lattice of MATBG, where for $M = 0$, the renormalized band

structure will contain perfectly flat f bands and non-Fermi liquid behavior.

V. MEAN-FIELD APPROACH

We follow the method of Florens and Georges [75,76] using an auxiliary-rotor description to develop a mean-field theory. The advantage of this approach is that it reproduces the correct strong- and weak-coupling limits and is not limited to a particular range of filling factors, enabling us to capture the valence fluctuations and Kondo effect in MATBG at all filling factors.

The auxiliary-rotor approach follows the strategy of earlier auxiliary boson methods separating the physical f-electron field into a product of a spin fermion and an ancillary charge boson, which in this case is represented as a rotor. The physical Hilbert space of $n = \nu + 4$ f electrons is represented as the product of a spinon and rotor state as follows:

$$|f^{\nu+4}\rangle = |\tilde{f}^{\nu+4}\rangle|\nu\rangle \quad (\nu \in [-4, 4]), \tag{40}$$

where $|\nu\rangle$ is an angular momentum eigenstate of a rotor with $L_z = \nu$, i.e., $\hat{L}^z|\nu\rangle = \nu|\nu\rangle$. We can rewrite $|\nu\rangle$ in the angular basis, $\langle\theta|\nu\rangle = e^{i\nu\theta}$, where

$$|\theta\rangle = \sum_\nu |\nu\rangle\langle\nu|\theta\rangle = \sum_\nu |\nu\rangle e^{-i\nu\theta}. \tag{41}$$

In this representation, the physical f-electron field is separated into a product of a spin fermion and an ancillary raising operator $L_+ = \sum_\nu |\nu+1\rangle\langle\nu|$:

$$f^\dagger_{\alpha\eta\sigma} \equiv \tilde{f}^\dagger_{\alpha\eta\sigma} L^+, \tag{42}$$

so that, each time an f fermion is added, the rotor angular momentum increases by one, conserving the gauge charge

$$\hat{Q} = \hat{\nu}_f - L^z, \qquad [f^\dagger_{\alpha\eta\sigma}, \hat{Q}] = 0, \tag{43}$$

where $\hat{\nu}_f = \hat{n}_f - 4$ is the filling factor. The physical Hilbert space corresponds to the gauge "neutral" slice of Fock space where $\hat{Q} = 0$, or $\nu_f = L^z$. Importantly, the constraint is a perfect constant of motion, so that the fluctuations in the rotor angular momentum perfectly track the fluctuations in the physical charge. For this reason, merely by imposing the constraint $\langle\hat{Q}\rangle = 0$, one obtains a good approximation to the underlying Coulomb blockade physics.

In the angular basis,

$$L^+|\theta\rangle = \sum_\nu |\nu+1\rangle e^{-i\nu\theta} = \sum_\nu |\nu\rangle e^{-i(\nu-1)\theta} = e^{i\theta}|\theta\rangle, \tag{44}$$

so that $L^+ = e^{i\theta}$ is simply a phase factor, and we can rewrite physical creation operator (42) as a product of spin and charge degrees of freedom:

$$f^\dagger_{\alpha\eta\sigma} \to \tilde{f}^\dagger_{\alpha\eta\sigma} e^{i\theta}. \tag{45}$$

In this way, the phase of the rotor θ is conjugate to the physical charge $n_f = -i(\partial/\partial\theta)$ of the f state.

With these considerations, the moiré atomic interaction (18) becomes

$$H_A = \frac{U}{2}\sum_{\mathbf{R}} (L^z_{\mathbf{R}} - \kappa\nu)^2, \tag{46}$$

while the hybridization (47) becomes

$$H_{fc} = \gamma_0 \sum_{\mathbf{R}\alpha\eta\sigma} \left(\tilde{f}^\dagger_{\mathbf{R}\alpha\eta\sigma} c_{\mathbf{R}\alpha\eta\sigma} L^+_{\mathbf{R}} + \text{H.c.} \right). \tag{47}$$

The mean-field theory is obtained by imposing $\langle Q\rangle = 0$ with a Lagrange multiplier, treating the rotor and fermionic degrees of freedom as separate degrees of freedom subject to this constraint. With this approximation, the hybridization is renormalized:

$$\gamma_0 \to \gamma = \gamma_0 \langle L^+_{\mathbf{R}}\rangle = \gamma_0 \langle e^{i\theta}\rangle \to \gamma_0 \langle \cos\theta\rangle, \tag{48}$$

where, for convenience, one chooses a phase where $\langle \sin\theta\rangle = 0$. The coupling between the fermions and the rotor defined by H_{fc} produces a transverse Weiss field on the rotor, giving rise to a mean-field rotor Hamiltonian of the following form:

$$H_{\text{rot}} = \frac{U}{2}(L_z - \kappa\nu)^2 - K\cos\theta \tag{49}$$

subject to the constraint

$$K = -2\gamma_0 \langle \tilde{f}^\dagger_{\mathbf{R}\alpha\eta\sigma} c_{\mathbf{R}\alpha\eta\sigma}\rangle. \tag{50}$$

We now reformulate the mean-field theory as a variational Hamiltonian, rewriting the lattice Hamiltonian (1) as

$$H = H_{\text{rot}} + H_F + N_s\left(\frac{\gamma K}{\gamma_0} + \mu\nu\right), \tag{51}$$

$$H_{\text{rot}} = N_s\left[\frac{U}{2}L_z^2 - (\xi + U\kappa\nu)L_z - K\cos\theta\right], \tag{52}$$

$$H_F = \sum_{\mathbf{k}\eta\sigma}\left[\Psi^\dagger_{\mathbf{k}\eta\sigma}\mathcal{H}_{\text{F}}(\mathbf{k})\Psi_{\mathbf{k}\eta\sigma}\right] + \mu\langle N_c\rangle_{\nu=0} - N_s(\xi-\mu)N_f, \tag{53}$$

where γ, K, and ξ are determined by the stationary points of the mean-field free energy. Note that the cross term $N_s(\gamma K/\gamma_0)$ in H results from a Hubbard-Stratonovich decoupling of the hybridization (47), permitting us to vary γ and K independently, using stationarity to impose the constraints (48) and (50). The matrix

$$\mathcal{H}_F(\mathbf{k}) = \begin{pmatrix} (\xi-\mu)\sigma_0 & \gamma\phi^{(\eta)}(\mathbf{k}) & \cdots & \gamma\phi^{(\eta)}(\mathbf{k}+\mathbf{G}_n) \\ \gamma\phi^{(\eta)}(\mathbf{k})^\dagger & \mathcal{H}^{(\eta)}(\mathbf{k})-\mu\underline{1} & 0 & 0 \\ \vdots & 0 & \ddots & 0 \\ \gamma\phi^{(\eta)}(\mathbf{k}+\mathbf{G}_n)^\dagger & 0 & \cdots & \mathcal{H}^{(\eta)}(\mathbf{k}+\mathbf{G}_n)-\mu\underline{1} \end{pmatrix} \tag{54}$$

determines the quasiparticle dispersion with renormalized hybridization strength γ, where the conduction electron dispersion matrix $\mathcal{H}^\eta(\mathbf{k})$ is defined in Eq. (6) and the hybridization matrices $\phi^{(\eta)}(\mathbf{k})$ defined in Eq. (9). $\langle N_c\rangle_{\nu=0}$ is the number of c electrons at half filling, and $N_f = 4$ is the valley spin degeneracy. L_z is the angular momentum operator. We rewrite the rotor Hamiltonian as

$$H_{\rm rot} = \frac{U}{2}L_z^2 - (\xi + U\kappa\nu)L_z - \frac{K}{2}(L_+ + L_-). \tag{55}$$

ξ is the Lagrange multiplier that constrains the allowed values of the angular momentum component $L_z = m_l \in [-N_f, N_f]$.

$$\Psi_{\mathbf{k}\eta\sigma} = (\tilde{f}_{\mathbf{k}1\eta\sigma}, \tilde{f}_{\mathbf{k}2\eta\sigma}, c_{\mathbf{k}1\eta\sigma}, c_{\mathbf{k}2\eta\sigma}, c_{\mathbf{k}3\eta\sigma}, c_{\mathbf{k}4\eta\sigma}, c_{\mathbf{k}+\mathbf{G}_1 1\eta\sigma}, \ldots, c_{\mathbf{k}+\mathbf{G}_n 3\eta\sigma}, c_{\mathbf{k}+\mathbf{G}_n 4\eta\sigma})^T \tag{56}$$

is a spinor combining the four conduction fields at each reciprocal lattice vector and the two f-electron operators at each valley $\eta = \pm 1$ and spin $\sigma = \pm 1$. (For convenience, henceforth we drop the tilde on the f fields.) Notice that while $H_{MF}(\mathbf{k})$ commutes with the spin and valley quantum numbers, at general momentum it breaks the twofold Γ_3 degeneracy down to a $N_f = 4$-fold valley-spin degeneracy.

The mean-field Free energy per unit cell obtained by integrating out the fermions for a static configuration of the fields (γ, ξ, K) is then

$$\mathcal{F} = F + \Phi_{\rm rot} + \left(\frac{\gamma K}{\gamma_0} + \mu\nu\right), \tag{57}$$

$$F = -\frac{N_f}{N_s}T\sum_{\mathbf{k}}{\rm Tr}\ln(1 + e^{-\beta\mathcal{H}_F(\mathbf{k})}) + \mu\langle N_c\rangle_{\nu=0} - (\xi-\mu)N_f, \tag{58}$$

$$\Phi_{\rm rot} = -T\ln{\rm Tr}[e^{-\beta H_{\rm rot}}]. \tag{59}$$

Writing

$$\begin{aligned} -TN_f\sum_{\mathbf{k}}{\rm Tr}[1 + e^{-\beta\mathcal{H}_F(\mathbf{k})}] &= -TN_f\sum_{\mathbf{k}}{\rm Tr}[2\cosh(\beta\mathcal{H}_F(\mathbf{k})/2)] + \frac{N_f}{2}\sum_{\mathbf{k}}{\rm Tr}\mathcal{H}_F(\mathbf{k}) \\ &= -TN_f\sum_{\mathbf{k}}{\rm Tr}[2\cosh(\beta\mathcal{H}_F(\mathbf{k})/2)] + N_sN_f[(\xi-\mu) - \mu 2N_G] \\ &= -TN_f\sum_{\mathbf{k}}{\rm Tr}[2\cosh(\beta\mathcal{H}_F(\mathbf{k})/2)] + N_s(\xi-\mu)N_f - \mu\langle N_c\rangle_{\nu=0}, \end{aligned} \tag{60}$$

where N_G ($N_G = 7$ in our calculations) is the number of reciprocal lattice vectors $\vec{G}$, including the origin included in $\mathcal{H}_F$, we can rewrite the mean-field free energy per unit cell as

$$\mathcal{F} = -\frac{N_f}{N_s}T\sum_{\mathbf{k}}{\rm Tr}\ln\{2\cosh[\beta\mathcal{H}_F(\mathbf{k})/2]\} + \Phi_{\rm rot} + \left(\frac{\gamma K}{\gamma_0} + \mu\nu\right). \tag{61}$$

The saddle-point requirement that F be stationary with respect to variations in K, γ, and ξ imposes the coupled self-consistency conditions

$$\langle\cos\theta\rangle_\theta = \frac{\gamma}{\gamma_0}, \tag{62}$$

$$K = -2\frac{\gamma_0}{N_s}\sum_{\mathbf{R},B}\langle c^\dagger_{\mathbf{R}B}\tilde{f}_{\mathbf{R}B}\rangle, \tag{63}$$

and

$$\langle L_z\rangle = \frac{1}{N_s}\sum_{\mathbf{R},B}\langle\tilde{f}^\dagger_{\mathbf{R}B}\tilde{f}_{\mathbf{R}B}\rangle - N_f = \nu_f. \tag{64}$$

Stationarity of the free energy with respect to the chemical potential μ fixes the total number of electrons N_e in the system:

$$-\frac{\partial \mathcal{F}}{\partial \mu} = \nu_c + \nu_f - \nu = 0, \tag{65}$$

where $\nu = (N_e - \langle N_e \rangle_{\nu=0})/N_s$ is the filling factor and we denote $\nu_c = (\langle \hat{N}_c \rangle - \langle \hat{N}_c \rangle_{\nu=0})/N_s$.

The key scales of the mean-field mixed valent moiré lattice model for TBG are set by the impurity physics before coherence is reached. Hence, the doping-temperature phase diagram for the mixed valent moiré lattice model would greatly resemble a Doniach phase diagram based on a single-impurity model for the f states in MATBG.

The mean-field hybridization width for the mixed valent moiré lattice is

$$\Delta[\mu] = \pi \rho_c(\mu) \overline{\gamma^2(k)}, \tag{66}$$

where $\overline{\gamma^2(k)} = [\gamma^2/(\gamma_0)^2]\overline{\gamma_0^2(k)}$ is the momentum integrated average of the mean-field hybridization squared. We anticipate the approximate mean-field bandwidth of the flat band to be

$$\tilde{W}_{\mathrm{MF}} = v_D^{\mathrm{MF}} K_\theta = \frac{\gamma^2}{(\gamma_0)^2} W \sim \Delta, \tag{67}$$

where v_D^{MF} is the Dirac velocity at the K_M points for the mean-field theory and W is the bare noninteracting bandwidth (68).

VI. MEAN-FIELD RESULTS

In our calculations, we adopt the phenomenological values $U = 30$ meV, $\kappa = 0.8$, and $\gamma_0 = 6.5$ meV. The choice of γ_0 is a delicate balance: If γ_0 is too large, then no local moment behavior survives and the chemical potential has no reset behavior; if γ_0 is too small, then the band gap between the flat bands and remote bands at Γ_M never fully opens and the flat bands never become topological. Our choice of γ_0 preserves the resetting behavior of the chemical potential $\mu[\nu]$ as a function of filling, at the cost of the gap to the remote bands from opening [103].

With these reduced bare parameters, the noninteracting bandwidth (29) is reduced to

$$W \approx 0.02M \sim 1.0 \text{ K}. \tag{68}$$

We then numerically solve the self-consistent equations (63)–(65) as a function of the filling factor. The particle-hole symmetric results are displayed for positive doping. With the choice of parameters above, our mean-field theory reproduces the moiré atomic limit (Sec. III B). The chemical potential μ undergoes a partial reset as a periodic function of filling (Fig. 11) and the inverse compressibility has peaks at integer fillings (Fig. 12), a consequence of the Coulomb blockade physics and the emergent f-electron potential. The scales from the analytic unhybridized moiré atomic limit [Fig. 6(a)] are renormalized in our mean-field results by both the finite hybridization and finite temperature effects.

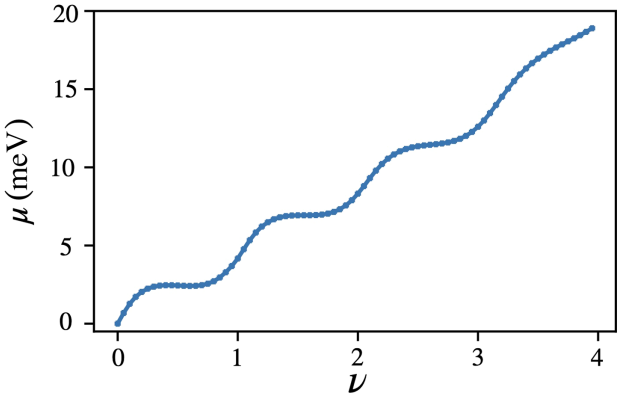

FIG. 11. Chemical potential μ variation with total filling factor ν for $T = 0.1$ meV with phenomenological parameters $U = 30$ meV and $\kappa = 0.8$ within the mean-field theory. Like the moiré atomic limit, the chemical potential jumps at the integer filling factors and partially resets between successive integer fillings. The analytic chemical potential of the jump by U and the partial reset by $U\kappa$ within the moiré atomic limit are renormalized by both finite hybridization and finite temperature effects.

A. Unquenched f states

We observe development of nonzero hybridization $\langle \cos\theta \rangle_\theta = \gamma/\gamma_0 \neq 0$ at a characteristic temperature $T_K^{(1)} \approx 9$ meV (Fig. 13), formally indicating the onset of the Kondo effect. This would typically signal the fractionalization of the local moments into heavy f states and the formation of a heavy Fermi liquid state below $T_K^{(1)}$ in conventional heavy-fermion systems.

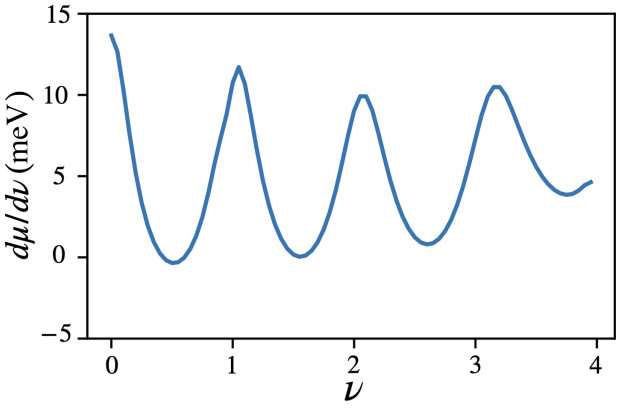

FIG. 12. Inverse compressibility $d\mu/d\nu$ variation with total filling factor ν for $T = 0.1$ meV with phenomenological parameters $U = 30$ meV and $\kappa = 0.8$ within the mean-field theory. Like the moiré atomic limit, we get small negative values around half-integer fillings. The scales from the moiré atomic limit are renormalized by both finite hybridization and finite temperature effects.

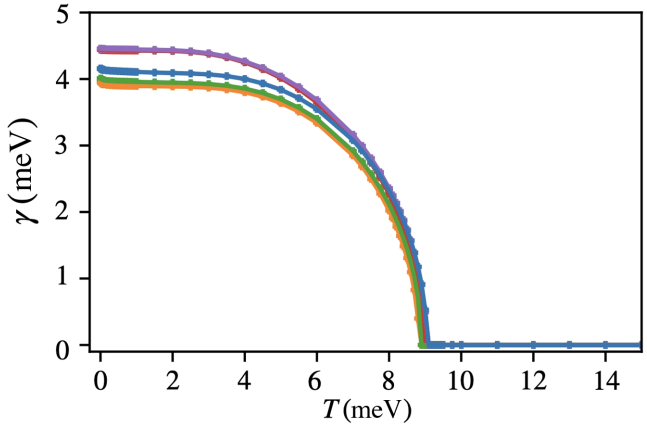

FIG. 13. Mean-field order parameter $\gamma(T)$ plotted against temperature for fillings $\nu = 0$ (orange), 0.5 (red), 1 (green), 1.5 (purple), and 2 (blue). We find the Kondo order transition $T_K^{(1)} \sim 9$ meV. Bare hybridization used: $\gamma_0 = 6.5$ meV.

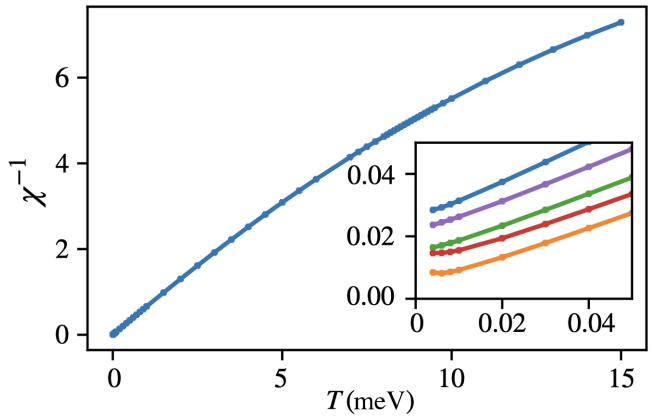

FIG. 14. Inverse spin and valley susceptibility χ^{-1} as a function of temperature T for integer filling $\nu = +2$ plotted in blue. There is a subtle crossover between two Curie-Weiss behaviors around the temperature $T_K^{(1)} \approx 9$ meV where Kondo order turns on. Inset: inverse spin and valley susceptibility for fillings $\nu = 0$ (orange), 0.5 (red), 1 (green), 1.5 (purple), and 2 (blue), offset by different constants for clarity. Curie-Weiss behavior persists well below the Kondo ordering temperature $T_K^{(1)}$, and magnetic SU(8) local moments in MATBG are fully screened only at around $T_K^{(2)} \sim 0.01$ meV, where Curie-Weiss behavior ends.

However, the relevant energy scale for Fermi liquid formation is the much smaller f-band width $\tilde{W}_{\rm MF}$ (67), which gives rise to a much lower coherence temperature $T_K^{(2)} \sim \tilde{W}_{\rm MF} \ll T_K^{(1)}$. This disparity leads to the persistence of thermally active, unquenched f states in the wide intermediate temperature range between $T_K^{(1)}$ and $T_K^{(2)}$. The signatures of these unquenched f states include a Curie-Weiss magnetic susceptibility down to $T_K^{(2)}$, local moments with an unquenched entropy that persists below $T_K^{(1)}$, and ultimately quenching below $T_K^{(2)}$, giving rise to a specific heat feature around $T_K^{(2)}$.

We calculate the magnetic susceptibility $\chi = -\partial^2 \mathcal{F}/\partial B^2$, evaluated at $B = 0$ from the bubble diagram of the f spinors, which is is equivalent to calculating $-\partial^2 \mathcal{F}/\partial \mu^2|_\xi$ at a fixed constraint field ξ. At high temperatures larger than the Kondo temperature, we expect the magnetic susceptibility to assume a Curie-Weiss form:

$$\chi(T) \propto \frac{m^2}{T + \theta}, \tag{69}$$

where m is the magnetic moment of each free local moment and θ is the Curie-Weiss temperature, a phenomenological scale taking care of interactions between moments.

Typically, in heavy-fermion systems, the onset of Kondo order (Fig. 13) at $T_K^{(1)}$ coincides with the end of Curie-Weiss magnetic susceptibility due to Kondo screening. Intriguingly, and distinct from conventional heavy-fermion phenomenology, our mean-field theory for MATBG finds that the Curie-Weiss behavior, characterized by the linear temperature dependence of the inverse magnetic susceptibility χ^{-1}, persists below the Kondo ordering temperature $T_K^{(1)}$ down to a much smaller Kondo coherence scale $T_K^{(2)}$ (Fig. 14 inset).

At the mean-field condensation temperature $T_K^{(1)}$, we observe a transition between two different Curie-Weiss behavior in the inverse magnetic susceptibility $\chi^{-1}(T)$, exhibiting an increased gradient below the mean-field ordering temperature $T_K^{(1)}$ (Fig. 14). The gradient of the inverse magnetic susceptibility is inversely proportional to the square of the magnetic moment of the free local moments (69). Hence, the gradient increase indicates a partial quenching of the SU(8) local moments at $T_K^{(1)}$.

To verify the partial screening of the SU(8) local moments at the mean-field transition temperature $T_K^{(1)}$ and their thermal nature until the f states are fully quenched at the Kondo coherence temperature $T_K^{(2)}$, we calculate the entropy of the f state:

$$S = -\sum_n (|\langle n|1_f\rangle|^2 + |\langle n|2_f\rangle|^2) \times (f_n \ln f_n + (1 - f_n) \ln (1 - f_n)) \tag{70}$$

by projecting the analytic entropy for the eigenstate $|n\rangle$ of the fermionic mean-field Hamiltonian $\mathcal{H}_F$ (54), onto $|1_f\rangle$, and $|2_f\rangle$, the two orbital eigenstates of the f state in the moiré atomic limit with zero hybridization to the c electrons. In Eq. (70), $f_n = f(E_n, T)$ is the Fermi-Dirac distribution.

We confirm the incoherent thermal nature of the f states in the intermediate temperature regime $T_K^{(2)} < T < T_K^{(1)}$ by comparing the f-state entropy with the high-temperature fermionic entropy of a thermal state for $\nu = 2$, where $p = 6/8$ of the eight f states are filled:

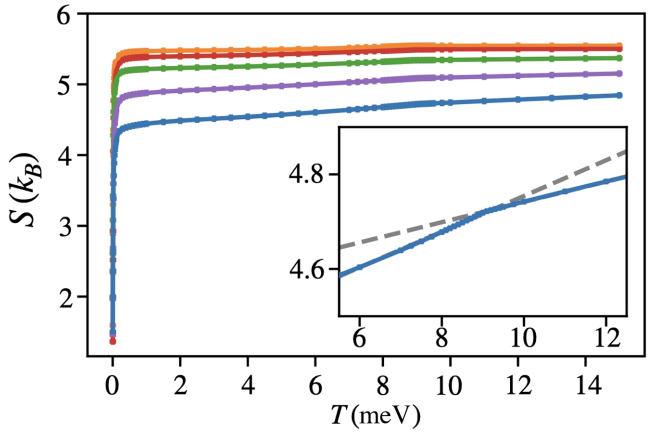

FIG. 15. Entropy S of the f states as a function of temperature T for fillings $\nu = 0$ (orange), 0.5 (red), 1 (green), 1.5 (purple), and 2 (blue). The entropy between $T_K^{(1)} \approx 9$ meV and $T_K^{(2)} \sim 0.01$ meV has good agreement with the high-temperature entropy $S_{\text{therm}} \approx 4.5k_B$ for a thermal state with six out of eight f states filled. Inset: enlarged view around the mean-field transition temperature $T_K^{(1)}$; dotted lines show a gradient decrease in the f-state entropy just below $T_K^{(1)}$.

$$S_{\text{therm}} = -8k_B(p \ln p + (1-p)\ln(1-p)) \approx 4.5k_B. \tag{71}$$

Our numerical results (Fig. 15) also show a good agreement with the thermal fermionic entropy (71) between $T_K^{(1)}$ and $T_K^{(2)}$ for the other filling factors, providing strong evidence that the f states remain thermalized and incoherent below the mean-field transition $T_K^{(1)}$, all the way down to the Kondo coherence temperature $T_K^{(2)}$.

We further calculate the f-state specific heat to temperature ratio by taking the temperature derivative of the f-state entropy S:

$$\frac{C_V}{T} = \frac{dS}{dT}. \tag{72}$$

At low temperatures, C_V/T is proportional to the effective mass of the quasiparticle carriers; in our numerical results, C_V/T peaks at a finite large value around the Kondo coherence temperature $T_K^{(2)}$ (Fig. 16), indicating that the coherent quasiparticle carriers are heavy.

B. Valence fluctuations

To show that our mean-field theory captures the valence fluctuations in the model, we calculate the distribution of valences as a function of filling. We do this by calculating the overlap between the ground state $|0_{\text{rot}}\rangle$ of the rotor Hamiltonian (55) using the mean-field parameters γ, λ, and K solved for self-consistently at $T = 0.1$ meV:

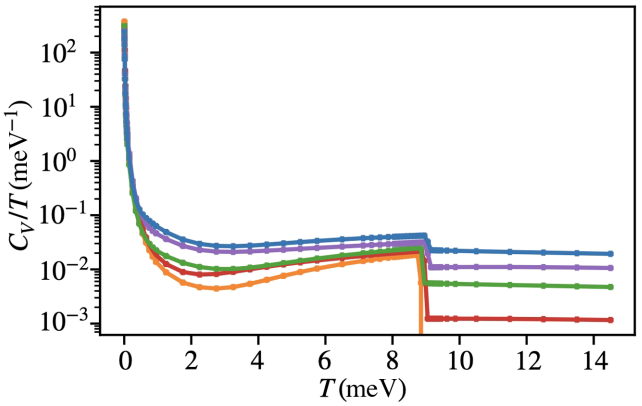

FIG. 16. Specific heat capacity divided by temperature C_V/T as a function of temperature T for fillings $\nu = 0$ (orange), 0.5 (red), 1 (green), 1.5 (purple), and 2 (blue). The discontinuous jump at $T_K^{(1)} \approx 9$ meV is a signature of the mean-field second-order phase transition for the Kondo phase. At the Kondo coherence temperature $T_K^{(2)} \sim 0.01$ meV, C_V/T peaks at a large finite value, a signature of the large effective mass of the quasiparticle carriers when coherence has formed.

$$P(Q) = |\langle Q|0_{\text{rot}}\rangle|^2, \tag{73}$$

where $|Q\rangle$ is the angular momentum eigenstate corresponding to valence Q and the probabilities are normalized such that $\sum_Q P(Q) = 1$. In the Kondo limit, $P(Q = 4 + \nu) = 1$, with no mixed valency.

As shown in Fig. 17, we observe a sharply peaked valence distribution at integer filling factors. In contrast, away from the integer filling factors, the probability of populating neighboring valence states (e.g., $Q = 3$, 5 for $\nu = 0$) becomes comparable to the probability of the central valence $\langle n_{f\mathbf{R}}\rangle = 4 + \nu$. This finding indicates the presence of strong valence fluctuations around half-integer filling

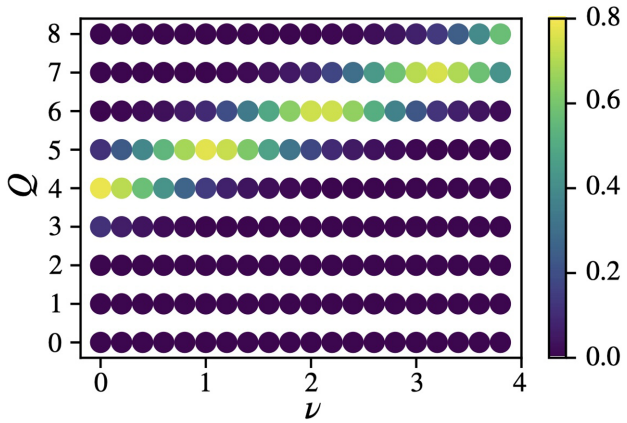

FIG. 17. Valence Q distribution of the f electrons as a function of filling ν; the color bar represents the probability of finding valence state Q at filling ν. Parameters used: $U = 30$ meV, $\kappa = 0.8$ with $\gamma_0 = 6.5$ meV at $T = 0.1$ meV.

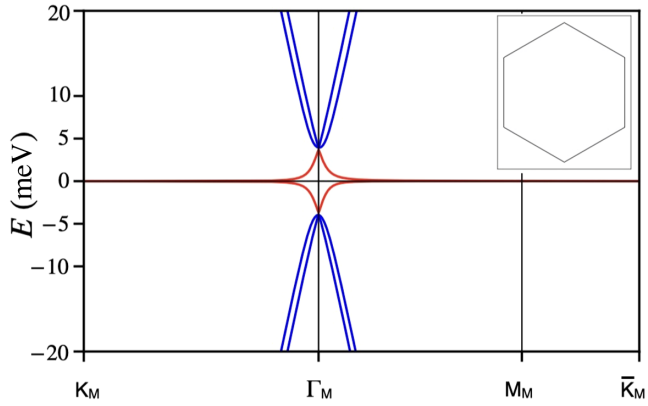

FIG. 18. Many-body mean-field band structure for a half filled flat band $\nu = 0$. Parameters used: chemical potential $\mu = 0$ meV, $\xi = 0$ meV, $U = 30$ meV, $\kappa = 0.8$, with $\gamma_0 = 6.5$ meV, and $\gamma = 3.96$ meV at $T = 0.004$ meV. The inset shows the Brillouin zone with no electron or hole pockets for half filling.

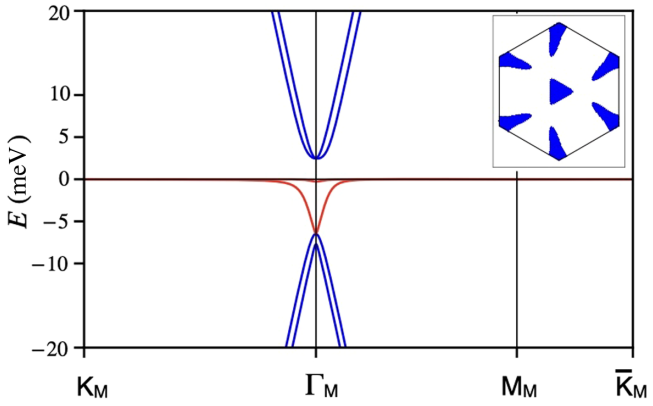

FIG. 20. Many-body mean-field band structure for $\nu = +1$. Parameters used: chemical potential $\mu = 3.99$ meV, $\xi = 4.01$ meV, $U = 30$ meV, $\kappa = 0.8$, with $\gamma_0 = 6.5$ meV, and $\gamma = 4.01$ meV at $T = 0.004$ meV. The inset shows the Brillouin zone with electron pocket relative to half filling, shaded in blue.

factors, despite the established of Kondo order at temperatures below $T_K^{(1)}$.

This mixed valence behavior departs from the prototypical Kondo limit, where a single well-defined valence state would dominate.

C. Quasiparticle band structures

We conclude the mean-field results section by showcasing the quasiparticle band structures (Figs. 18–22) for filling factors $\nu = \{0, +0.5, +1, +1.5, +2, \}$ at temperature $T = 0.004$ meV $\ll T_K^{(2)}$ below the Kondo coherence temperature.

The bandwidth of the mean-field quasiparticle dispersions (Figs. 18–22) at Γ_M remains at $2M$ but the bandwidth at K_M is renormalized down, causing the bands to be incredibly flat away from the Γ_M point. Using the

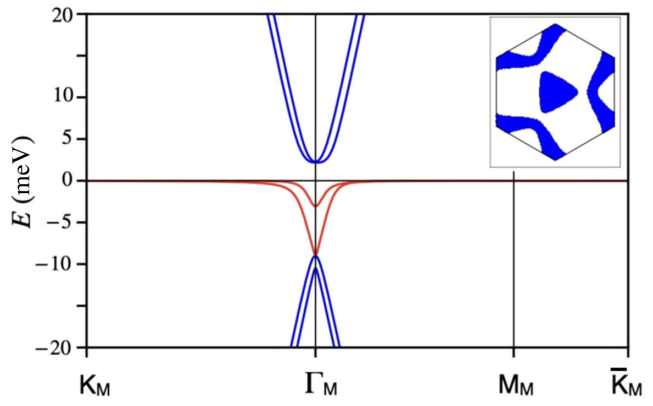

FIG. 21. Many-body mean-field band structure for $\nu = +1.5$. Parameters used: chemical potential $\mu = 6.77$ meV, $\xi = 6.82$ meV, $U = 30$ meV, $\kappa = 0.8$, with $\gamma_0 = 6.5$ meV and $\gamma = 4.46$ meV at $T = 0.004$ meV. The inset shows the Brillouin zone with electron pocket relative to half filling, shaded in blue.

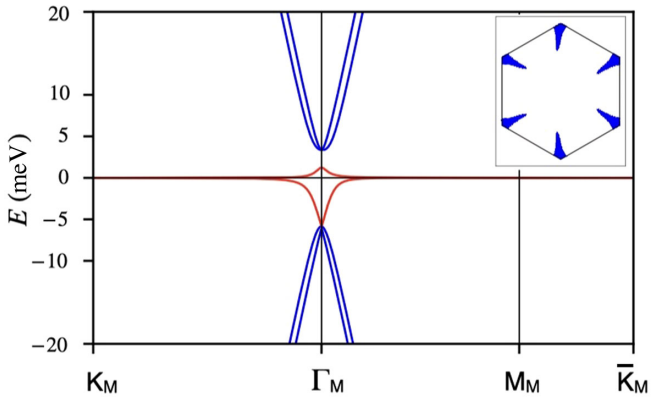

FIG. 19. Many-body mean-field band-structure for $\nu = +0.5$. Parameters used: chemical potential $\mu = 2.46$ meV, $\xi = 2.47$ meV, $U = 30$ meV, $\kappa = 0.8$, with $\gamma_0 = 6.5$ meV, and $\gamma = 4.45$ meV at $T = 0.004$ meV. The inset shows the Brillouin zone with electron pocket relative to half filling, shaded in blue.

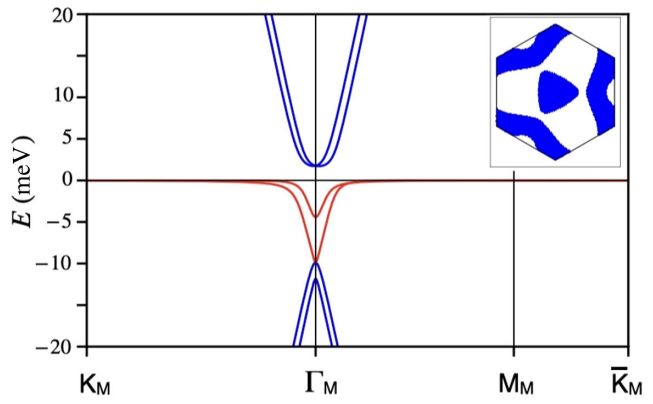

FIG. 22. Many-body mean-field band structure for $\nu = +2$. Parameters used: chemical potential $\mu = 8.13$ meV, $\xi = 8.18$ meV, $U = 30$ meV, $\kappa = 0.8$, with $\gamma_0 = 6.5$ meV and $\gamma = 4.16$ meV at $T = 0.004$ meV. The inset shows the Brillouin zone with electron pocket relative to half filling, shaded in blue.

renormalized mean-field hybridization $\gamma \approx 4$ meV at low temperatures (Fig. 13), we estimate the renormalized bandwidth at K_M (67) to be

$$\tilde{W}_{\rm MF} = v_D^{\rm MF} K_\theta \sim 0.01M \approx 0.03 \text{ meV} \approx 0.4 \text{ K}. \quad (74)$$

We find that the renormalized bandwidth $\tilde{W}_{\rm MF}$ is approximately a tenth of the bare bandwidth (29) and a good match to the Kondo coherence temperature $T_K^{(2)} \sim 0.01$ meV (Fig. 14) in our mean-field theory numerics.

VII. DISCUSSION

In this paper, we have investigated the Song-Bernevig model of twisted bilayer graphene, taking advantage of the close analogy with heavy-fermion and quantum dot physics. We have developed an auxiliary-rotor approach to describe the normal state across a full range of doping. Within the auxiliary-rotor approach, we are able to capture both the Kondo physics near integer filling factors and the strong mixed valency near half-integer filling factors. One of the key points to arise from our study are discrepancies between the *ab initio* values of the hybridization and on-site Coulomb interaction in the Song-Bernevig model and the corresponding values obtained from experiment. These discrepancies suggest renormalization processes, such as the effects of phonons, that may lie beyond the current model. Another key aspect of the physics is the presence of two scales in the problem—a nominal Kondo temperature which establishes the topological band structure and a much lower scale at which the flat bands lose their thermal entropy.

Further experiments may help to test the foundation of the SB description. In conventional heavy-fermion systems, the presence of local moment behavior is immediately evident from the Curie-Weiss behavior of the magnetic susceptibility

$$\chi(T) \propto \frac{1}{T+\theta}. \quad (75)$$

To what extent can such Curie-Weiss behavior be detected from a Maxwell analysis of field-dependent compressibility measurements? It would be useful to use field-dependent compressibility measurements to back out the spin and valley susceptibility and directly measure the size of the moment. It would also be intriguing, in future work, both theoretical and experimental, to observe and quantify the charge redistribution between the conduction and f electrons as a function of gate voltage.

Magnetic susceptibility measurements would be a key indicator of the predicted two Kondo temperatures ($T_K^{(1)}$ and $T_K^{(2)}$). A key issue is whether MATBG exhibits a Pauli paramagnetic region (indicating a heavy Fermi liquid) or whether Curie paramagnetism persists down to superconductivity or correlated insulator transition temperatures, as in the heavy-fermion superconductors $NpPd_5Al_2$ and $CeCoIn_5$ [104].

The heavy-fermion physics in MATBG raises an interesting possibility of parallels between STM tunneling in MATBG and traditional heavy-fermion systems. The specific manifestation of Kondo behavior will depend on the position-dependent tunneling amplitudes into the conduction states (dominating at the AB points) and the f states (dominating at the AA points): The AB regions are expected to provide a broad feature characteristic of the Gamma-point light fermions, whereas the AA regions should image the very narrow V-shaped density of states of the coherent f states. Generically, as in conventional heavy fermions, we expect a Fano feature corresponding to the interference between conduction and f-state tunneling amplitudes [105]. The detailed form of Fano features and their dependence on the incoherent scattering that will persist between $T_K^{(1)}$ and $T_K^{(2)}$ are key issues for future investigation.

We note that our work does not yet include the effects of strain, particularly, "heterostrain," in which one layer is uniaxially strained relative to the other. Heterostrain is known to preserve the Dirac points, while breaking the degeneracy between the renormalized Dirac cones in the same valley [91,94]. Our two-temperature Kondo description is expected to remain valid in this situation, because each Dirac cone will be associated with its own renormalized Dirac bandwidth, and the chemical potential will lie close to the K_M or $\overline{K}_M$ Dirac cone, depending on whether the system is electron or hole doped. This increased Dirac bandwidth produced by heterostrain could, however, raise the lower Kondo temperature $T_K^{(2)}$ to the point where Fermi liquid behavior becomes apparent. Furthermore, the reduction of nonlocal interactions relative to on-site terms by heterostrain [94] would provide additional support for the use of a simplified treatment of local interactions model.

Although the work of Song and Bernevig emphasizes an *ab initio* description of the relevant interactions in MATBG, giving rise to an on-site Coulomb interaction in the range 60–100 meV, the measured $U \sim 30$ meV [50] is significantly smaller, suggesting that there are important renormalization effects at work in the low-energy physics of MATBG. A similar discrepancy is implicit in DMFT approaches to MATBG [23,47], which have encoded the discrepancy in terms of a dielectric constant $\epsilon \sim 10$, a factor of 2 or 3 larger than the accepted value for this system.

A promising candidate for these renormalization effects are the interactions of phonons with the valence fluctuations, an effect which we now briefly discuss. Recent μ-ARPES experiments [87] have demonstrated a coupling of the flat f bands with an intervalley optic phonon (Fig. 23) that gives rise to multiple satellites in the density of states, separated by the optic K-phonon frequency of about $\omega_0 \sim 150$ meV. These phonons modify the moiré

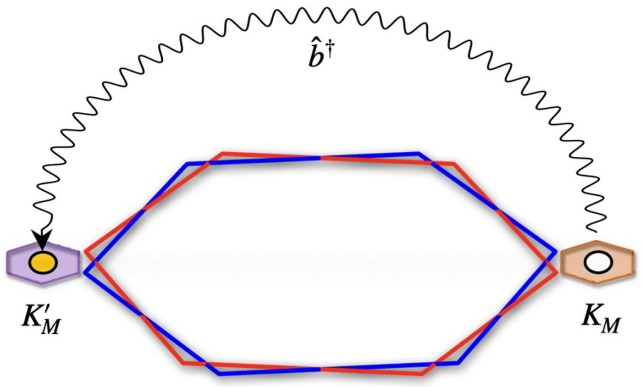

FIG. 23. Schematic representation of the K-phonon process, whereby an f electron in the valley K_M is scattered to the other valley K'_M through the absorption or emission of a K phonon.

atomic Hamiltonian of the flat-band electrons in MATBG, giving rise to a Holstein model of the form

$$H = \omega_0 b^\dagger b + g(b + b^\dagger) f^\dagger \tau_x f, \tag{76}$$

where τ_x denotes the valley spin operator and we have modeled the optic phonon as a single Einstein mode. From this Hamiltonian, we see that the valley spin of the f electrons acts as a force term on the optic phonons. Each time an f electron is added to the system, the phonons will valley polarize. Moreover, since the frequency of the Einstein mode is far greater than the characteristic timescales of valence fluctuations, this polarization will have time to fully establish itself each time the valence fluctuates. Such polaronic effects are usually negligible in heavy-fermion systems, where the valence fluctuations are far faster than the phonons [85,86], and have recently been observed to develop in conjunction with the slow charge fluctuations associated with strange-metal behavior in the heavy-fermion compound $YbAlB_4$ [106]. Suppose we add an f electron into a coherent superposition of valleys, forming a state $|f^1, \tau_x = 1\rangle$; then, the resulting bosonic ground state is a Glauber state given by

$$|b\rangle = e^{-|z|^2/2} e^{-z b^\dagger} |0\rangle, \tag{77}$$

where $z = (g/\omega_0)\tau_x$. In fact, we can replace $z \to \sqrt{n_b}$, where n_b is the number of bosons that condense in response to the valence fluctuation. From this simple argument, we see that the f-quasiparticle operator for this system must also include the coherent state term of the bosons, i.e.,

$$f^\dagger_{qp} = e^{-n_b/2} e^{-\sqrt{n_b}(f^\dagger \tau_x f) b^\dagger} f^\dagger, \tag{78}$$

where we have dropped the valley spin indices. The overlap between an unrenormalized f state and the quasiparticle is then $\sqrt{Z} = \langle f_{qp} | f^\dagger | 0 \rangle = e^{-n_b/2}$. This immediately implies that both the hybridization and the repulsive U will be renormalized as follows:

$$\gamma_0 \to \gamma_0^* = \sqrt{Z}\gamma_0, \qquad U \to U^* = Z^2 U. \tag{79}$$

Experiment indicates that $U^*/U \sim 1/4$, implying that $Z \sim 1/2$ corresponding to $n_b = \ln 2 \sim 0.7$ valley phonons associated with each additional f electron.

Our auxiliary-rotor mean-field approach necessitated a reduction of the bare hybridization from $\gamma_0 = 25$ meV to $\gamma_0 = 6.5$ meV—exceeding the expected polaron renormalization [Eq. (79)]—to preserve the resetting behavior of the chemical potential $\mu[\nu]$ as a function of filling. We attribute this to the method's overestimation of the physical problem's relevant cutoff, yielding $D = 133$ meV instead of $U/2 = 15$ meV. We leave this to be addressed in future studies.

We note following previous authors [107–111] that, in addition to the renormalization of the Coulomb interaction, the valley phonon will introduce an attractive Valley-Hunds interaction of the form $H_{ph} = -(g^2/\omega_0)(f^\dagger \tau_x f)^2$. In fact, when we normal order this interaction, we obtain

$$H_{ph} = -\frac{g^2}{\omega_0}[n_f + :(f^\dagger \tau_x f)^2:\,]. \tag{80}$$

The first term in this expression is a local binding potential which provides a natural contribution to the heavy-fermion binding potential we have introduced in this paper, on purely phenomenological grounds, allowing us to tentatively identify

$$\kappa U = \frac{g^2}{\omega_0}. \tag{81}$$

Based on the model fitting the μ-ARPES data [87], we obtain $\kappa \sim 0.6$, which is in the right ballpark for our mean-field theory. However, estimating κ through electron-phonon coupling strengths from the literature poses a challenge for two reasons. First, the relevant coupling is between optical phonons and localized electron states at the AA sites, whereas *ab initio* results typically address Bloch states and acoustic phonons. Second, reported coupling strengths vary widely in the literature.

The coupling strength required to obtain $\kappa = 0.8$, $g \approx 60$ meV lies between literature extremes: an order of magnitude above some electron-phonon couplings [112]—which consider only phonon frequencies in an energy window smaller than the 150 meV optical K phonon, yet an order of magnitude below Bloch electron-optical K-phonon couplings [109]. A recent study of optical K phonons coupled to AA-localized states suggests lower coupling values but acknowledges significant parameter sensitivity [110]. It would be interesting in future studies to use the μ-ARPES satellite data [87] to fit g and predict κ. Several authors have

commented on the possibility for the second term of Eq. (80) to play an important role in the superconductivity of MATBG. The full implications of this line of reasoning will be explored in our future work.

A second key aspect of our study is the presence of two Kondo scales for the MATBG Kondo lattice—a large separation between the Kondo temperature $T_K^{(1)}$ associated with the Withoff-Fradkin fixed point, which establishes the topology in the flat bands, and a considerably lower coherence temperature $T_K^{(2)}$, at which the flat bands entangle with the conduction sea and lose their thermal entropy, forming a heavy Fermi liquid (see Fig. 10). This finding is consistent with an extensive temperature regime hosting a two-fluid system [113] comprising coherent hybridized electrons at the Γ point and thermal flat f states around the K_M points. Our mean-field theory provides the following estimates for the two scales [see Eqs. (37) and (38)]:

$$T_K^{(1)} \sim \gamma, \qquad T_K^{(2)} \sim B\left(\frac{T_K^{(1)}}{K_\theta v_\star}\right)^2 M, \tag{82}$$

where $B = 2(1 + a_\star^2 K_\theta^2) + \tilde{\lambda}^2(1 - a_\star^2 K_\theta^2) \sim 10$ is a dimensionless factor and our estimate of the lower Kondo temperature $T_K^{(2)}$ is the renormalized Dirac bandwidth around the moiré K points (67).

Although we can only crudely estimate $T_K^{(1)} \sim \gamma \sim$ 50–100 K, i.e., $T_K^{(1)}/(v_\star K_\theta) \sim 1/100$, so that $T_K^{(2)} \sim M/100 \sim 0.5$ K, the important point is that the high-temperature Kondo crossover will dominate most of the measured temperature range. Indeed, it is likely that true Fermi liquid behavior is interrupted by superconductivity or insulating behavior—i.e., the Kondo I fixed point dominates most of the interesting temperature range—and that the Fermi liquid limit is never actually attained.

We now discuss some of the implications of our of our model for electron transport properties. Below $T_K^{(1)}$, we expect that, as the temperature decreases due to the hybridization between the local moments and the c electrons develops, the gap from the flat-band edge to remote bands will open and widen. In a conventional Fermi liquid, the inelastic electron scattering rate is governed by the phase space for three-quasiparticle excitations, which grows as the square of the energy ω^2:

$$\tau_{FL}(\omega) \propto \int_0^\infty d\epsilon_1 d\epsilon_2 d\epsilon_3 \delta(\omega - \epsilon_1 - \epsilon_2 - \epsilon_3) \propto \omega^2, \tag{83}$$

which at finite temperature leads to a T^2 scattering rate. However, our theory indicates that, in MATBG, at temperatures that lie between the two widely separated scales $T_K^{(1)}$ and $T_K^{(2)}$, the flat-band electrons are thermalized. For these electrons, the main dissipation process will involve scattering into an intermediate state containing a particle-hole pair of electrons near the Γ point. The phase space for this process involves one intermediate f state at $\epsilon_3 = 0$ and two rapidly dispersing electrons near the Γ point at energies ϵ_1 and ϵ_2, with a corresponding phase space

$$\tau_{\mathrm{NFL}}(\omega) \propto \int_0^\infty d\epsilon_1 d\epsilon_2 d\epsilon_3 \delta(\omega - \epsilon_1 - \epsilon_2 - \epsilon_3)\delta(\epsilon_3) \propto \omega, \tag{84}$$

that is now linear in energy. When thermal factors are included, this leads to a scattering rate that is linear in temperature and energy: a marginal Fermi liquid [114]. This observation raises an intriguing prospect that the strong-coupling fixed point created by Withoff-Fradkin scaling, with thermal flat-band f states, might provide the essential phase space for the strange-metal T-linear resistivity observed in MATBG. This is an interesting topic for future study. One of the other curious features of our model is that the decay of a flat-band fermion into three light fermions will exhibit a T^2 scattering rate, which may explain the curious observation of at T^2 Hall angle [13]—a feature that is absent in an electron-phonon model [115] for the strange-metal behavior.

ACKNOWLEDGMENTS

This work was supported by Office of Basic Energy Sciences, Material Sciences and Engineering Division, U.S. Department of Energy (DOE) under Contract No. DE-FG02-99ER45790 (L. L. H. L. and P. C.). We gratefully acknowledge discussions with Eva Andrei, B. Andrei Bernevig, Premi Chandra, Shahal Ilani, Daniel Kaplan, Xi Dai, Eslaf Khalaf, Alexei Tsvelik, Roser Valenti, Nikhil Tilak, and Zhenyuan Zhang.

APPENDIX A: COULOMB ENERGY WITH SCREENING

Here, we evaluate the Coulomb integral (15)

$$U = \int_{\mathbf{x},\mathbf{x}'} \rho(\mathbf{x}) V(\mathbf{x} - \mathbf{x}') \rho(\mathbf{x}'), \tag{A1}$$

where

$$\rho(\mathbf{x}) = \frac{e^{-x^2/\lambda^2}}{\pi\lambda^2} \tag{A2}$$

is normalized electron density in the Wannier state and

$$V(\mathbf{x} - \mathbf{x}') = \frac{e^2}{4\pi\epsilon\epsilon_0} \sum_n \frac{(-1)^n}{\sqrt{|\mathbf{x} - \mathbf{x}'|^2 + (2dn)^2}} \tag{A3}$$

is the screened Coulomb interaction between electrons, where d is the distance to the back gate(s). The summation $\sum_{n=0,1}$ for a single back gate with a single image charge per electron and $\sum_{n=-\infty}^{\infty}$ for a double back gate, where there are the multiply reflected image charges of alternating sign.

The result of the integral (A4) is

$$U = U_0 F\left[\frac{d}{\lambda}\right], \tag{A4}$$

where

$$U_0 = \sqrt{\frac{\pi}{2}}\frac{e^2}{4\pi\epsilon_0\epsilon\lambda} \tag{A5}$$

is the unscreened Coulomb interaction and

$$F[x] = \sum_n (-1)^n e^{2xn^2}\mathrm{Erfc}[\sqrt{2}xn] \tag{A6}$$

describes the dependence of the screening on the distance to the back gate. For a single back gate $\sum_n = \sum_{n=0,1}$, while for a double back gate, the sum is over all integers so that

$$F[x] = \begin{cases} 1 - e^{2x^2}\mathrm{Erfc}[\sqrt{2}x], & \text{single back gate,} \\ 1 + 2\sum_{n=1}^{\infty}(-1)^n e^{2x^2n^2}\mathrm{Erfc}[\sqrt{2}xn], & \text{double back gate.} \end{cases} \tag{A7}$$

To obtain Eq. (A4), we first substitute Eqs. (A2) and (A3) into Eq. (A1) to obtain

$$U = \frac{e^2}{4\pi\epsilon_0\epsilon}\int d^2x d^2x' \frac{1}{(\pi\lambda^2)^2} e^{-(x^2+x'^2)/\lambda^2}\sum_n \frac{(-1)^n}{\sqrt{|\mathbf{x}-\mathbf{x}'|^2 + (2dn)^2}}. \tag{A8}$$

Changing variables to $\mathbf{R} = (\mathbf{x}+\mathbf{x}')/2$ and $\mathbf{r} = \mathbf{x}-\mathbf{x}'$, so that $d^2x d^2x' = d^2r d^2R$, we have

$$U = \frac{e^2}{4\pi\epsilon_0\epsilon}\int d^2r d^2R \frac{1}{(\pi\lambda^2)^2} e^{-(4R^2+r^2)/2\lambda^2}\sum_n \frac{(-1)^n}{\sqrt{r^2 + (2dn)^2}}. \tag{A9}$$

Replacing $d^2r \to 2\pi r dr$ and $d^2R \to 2\pi R dR$, carrying out the first integral, we obtain

$$\begin{aligned} U &= \frac{e^2}{4\pi\epsilon_0\epsilon}\overbrace{\int_0^\infty \frac{2\pi R dR}{\pi\lambda^2} e^{-2R^2/\lambda^2}}^{1/2}\int_0^\infty \frac{2\pi r dr}{\pi\lambda^2} e^{-r^2/2\lambda^2}\sum_n \frac{(-1)^n}{\sqrt{r^2+(2dn)^2}} \\ &= \frac{e^2}{4\pi\epsilon_0\epsilon}\int_0^\infty \frac{r dr}{\lambda^2} e^{-r^2/2\lambda^2}\sum_n \frac{(-1)^n}{\sqrt{r^2+(2dn)^2}} \\ &= \frac{e^2}{4\pi\epsilon_0\epsilon}\int_0^\infty du e^{-u}\sum_n \frac{(-1)^n}{\sqrt{2\lambda^2 u + (2dn)^2}} = \frac{1}{\sqrt{2}}\frac{e^2}{4\pi\epsilon_0\epsilon\lambda}\sum_n (-1)^n \int_0^\infty du \frac{e^{-u}}{\sqrt{u+an^2}}, \end{aligned} \tag{A10}$$

where we substitute $u = r^2/2\lambda^2$ and set $a = 2(d^2/\lambda^2)$. Carrying out the final integral,

$$\int_0^\infty du \frac{e^{-u}}{\sqrt{u+an^2}} = \sqrt{\pi}e^{an^2}\mathrm{Erfc}[\sqrt{a}n], \tag{A11}$$

we obtain the results in Eqs. (A4)–(A6).

APPENDIX B: RENORMALIZED ANDERSON MODEL: COULOMB BLOCKADE PHYSICS AND CHEMICAL POTENTIAL

Here, we present the detailed analysis of the variation in chemical potential with filling factor as described in Sec. III B. Let us consider the variation of the chemical potential μ as a function of filling factor ν in an atomic model:

$$H_A(\mathbf{R}) = \frac{U}{2}(\hat{n}_{\mathbf{R}} - 4)^2 - U\kappa\nu\hat{n}_{\mathbf{R}} - \mu\hat{n}_{\mathbf{R}}, \tag{B1}$$

where $-U\kappa\nu$ is a phenomenological heavy-fermion potential proportional to the back-gate voltage. We rewrite the atomic Hamiltonian (B1) as the following:

$$H_A(\mathbf{R}) = \frac{U}{2}(\hat{n}_{\mathbf{R}} - 4 - \kappa\nu)^2 - \mu\hat{n}_{\mathbf{R}} \tag{B2}$$

and ignoring constant offsets to the Hamiltonian. The physics here is similar to a quantum dot. The stability of the quantum dot with $n = Q$ electrons requires the ionization energies

$$\begin{aligned}\Delta E_{\pm}^{Q} &= E_{Q\pm1} - E_{Q} \\ &= \frac{U}{2}(Q \pm 1 - 4 - \kappa\nu)^2 - \mu(Q \pm 1) \\ &\quad - \frac{U}{2}(Q - 4 - \kappa\nu)^2 + \mu Q \\ &= \frac{U}{2} \pm (U(Q-4) - U\kappa\nu - \mu) \\ &= \frac{U}{2} \pm (U(1-\kappa)\nu - \mu), \end{aligned} \tag{B3}$$

to be positive, where in the last line we use that the filling factor is defined as $\nu = Q - 4$. The ionization energies are positive provided that the chemical potential satisfies

$$\frac{U}{2} > |U(1-\kappa)\nu - \mu|. \tag{B4}$$

At integer filling factor ν, the chemical potential jumps from $-U/2 + U(1-\kappa)\nu$ to $U/2 + U(1-\kappa)\nu$ to compensate for the extra Coulombic cost. As the filling factor ν is tuned continuously from $\nu \to \nu + 1$, the emergent heavy-fermion potential compensates for $U\kappa$ of the Coulombic cost; hence, the chemical potential drops by the same amount $U\kappa$ to maintain the filling of the localized state. We now consider two extreme cases: the capacitive ($\kappa = 0$) and traditional heavy fermion ($\kappa = 1$). For the capacitive scenario (Fig. 24), there is no emergent heavy-fermion potential on the AA sites; therefore, the chemical potential has to bear the full Coulombic cost $\Delta\mu = U$ when the filling factor is increased by one $\Delta\nu = 1$. For a traditional heavy-fermion system ($\kappa = 1$, Fig. 25), neutrality shifts due to the perfect compensation of the Coulombic costs by the heavy-fermion potential, provided by protons in the nucleus. Consequently, there is no shift in the chemical potential $\Delta\mu = 0$ when the filling factor is increased by one $\Delta\nu = 1$.

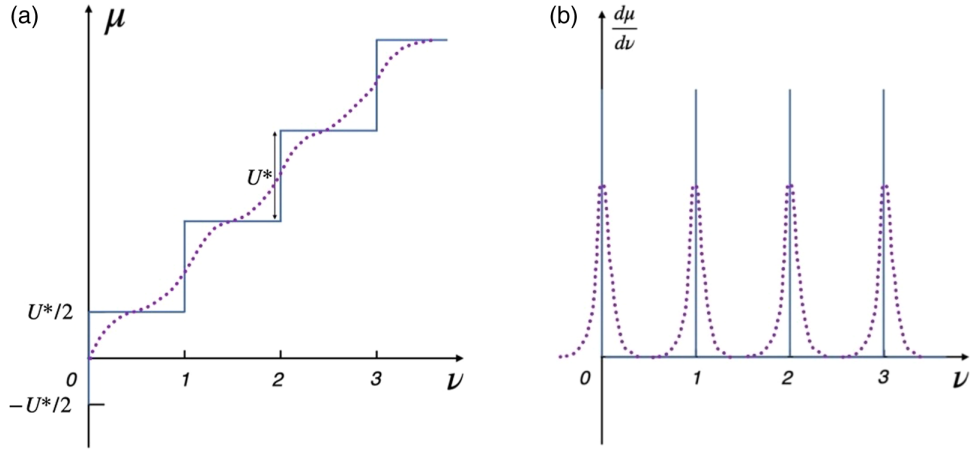

FIG. 24. Sketch in blue of (a) the chemical potential μ and (b) the inverse compressibility $d\mu/d\nu$ as functions of filling factor ν for the atomic limit of the renormalized Anderson model at zero temperature with $\kappa = 0$. There is no effective heavy-fermion potential, and the chemical potential jumps by U at each integer filling factor to compensate for the Coulombic cost of filling an extra atomic state. The inverse compressibility remains positive in this model.

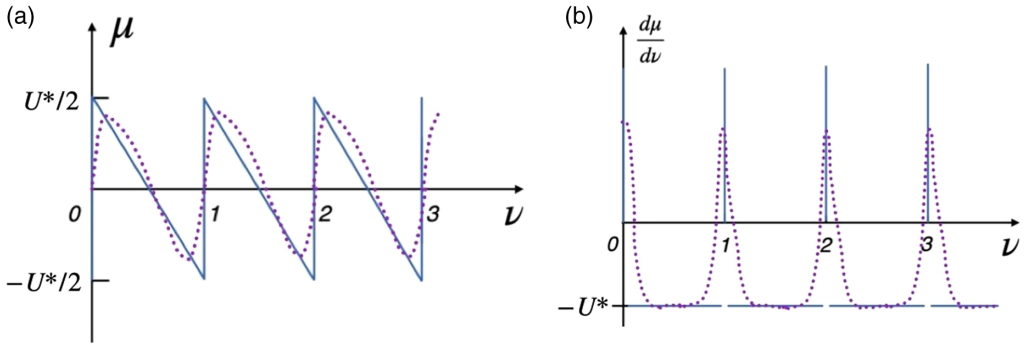

FIG. 25. Sketch in blue of (a) the chemical potential μ and (b) the inverse compressibility $d\mu/d\nu$ as functions of filling factor ν for the atomic limit of the renormalized Anderson model at zero temperature with $\kappa = 1$. The effective heavy-fermion potential perfectly compensates for the Coulombic cost for filling an extra atomic state; hence, the chemical potential completely resets at each integer filling factor. The inverse compressibility can take negative values of the order of $-U$ in this model.

APPENDIX C: DERIVATION OF THE FLAT-BAND DIRAC VELOCITY IN THE SONG-BERNEVIG MODEL

Here, we derive the approximate expression (22) for the Dirac velocity

$$v_D \approx 3\left(\frac{\gamma_K}{D}\right)^2 \frac{M}{D}\left(2(1+a_\star^2 K_\theta^2)+\tilde{\lambda}^2(1-a_\star^2 K_\theta^2)\right)v_\star \tag{C1}$$

at the K_M points of the Song and Bernevig model,

$$H_0 = \sum_{\mathbf{k}'\in \frac{\mathrm{MBZ}}{\mathbf{G}}}\Bigg[\sum_{aa'\eta\sigma}\mathcal{H}^{(\eta)}_{a,a'}(\mathbf{k}'-\mathbf{G})c^\dagger_{\mathbf{k}-\mathbf{G},a\eta\sigma}c_{\mathbf{k}'-\mathbf{G},a'\eta\sigma} + \frac{\gamma_0}{\sqrt{N_s}}\sum_{\alpha a\eta\sigma}([\phi^{(\eta)}(\mathbf{k}'-\mathbf{G},\gamma_0)]_{\alpha a}f^\dagger_{\mathbf{k}'\alpha\eta\sigma}c_{\mathbf{k}'-\mathbf{G},a\eta\sigma}+\mathrm{H.c.})\Bigg], \tag{C2}$$

where the conduction electrons can take momenta outside the moiré Brillouin zone and $\mathbf{G}$ are reciprocal lattice vectors. Here,

$$\mathcal{H}^{(\eta)}(\mathbf{k}) = \begin{pmatrix} & v_\star(\eta k_x\alpha_0 + ik_y\alpha_z) \\ v_\star(\eta k_x\alpha_0 - ik_y\alpha_z) & M\alpha_x \end{pmatrix}. \tag{C3}$$

The matrix form factor is

$$\phi^{(\eta)}(\mathbf{k}) \equiv \phi^{(\eta)}(\mathbf{k},\gamma_0) = e^{-k^2\lambda^2/2}\Big(\alpha_0 + a_\star(\eta k_x\alpha_x + k_y\alpha_y),\ 0_{2\times 2}\Big), \tag{C4}$$

where γ_0 and $a_\star$ set the magnitude and length scale of the hybridization and λ is a damping factor proportional to the real-space spread of the localized f-Wannier states. We also define the bandwidth $D = v_\star K_\theta$, $\tilde{\lambda} = \lambda K_\theta$ which will be useful later.

We focus on the physics at the K_M or $\bar{K}_M$ points and, since $\phi^{(\eta)}_{aa}(\mathbf{k})$ decays exponentially, we keep only the three MBZs surrounding the moiré K point, preserving the C_{3z} symmetry about that point (Fig. 26).

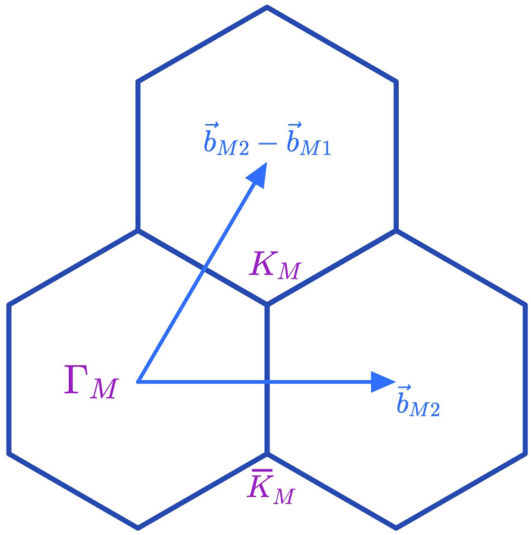

FIG. 26. Sketch of the three moiré Brillouin zones around the K_M point and the reciprocal lattice vectors.

Letting the eigenstates of the reduced model near the K_M point be

$$|\Psi(\delta\mathbf{k})\rangle = \Bigg(\sum_\alpha \psi^{(f)}_\alpha(\delta\mathbf{k})f^\dagger_{\mathbf{k}\alpha,\eta\sigma} + \sum_a\{\psi^{(0c)}_a(\delta\mathbf{k})c^\dagger_{\mathbf{k}a,\eta\sigma} + \psi^{(1c)}_a(\delta\mathbf{k})c^\dagger_{\mathbf{k}-\mathbf{G}_1,a,\eta\sigma} + \psi^{(2c)}_a(\delta\mathbf{k})c^\dagger_{\mathbf{k}-\mathbf{G}_2,a,\eta\sigma}\}\Bigg)\Big|_{\mathbf{k}=\mathbf{K}_M+\delta\mathbf{k}}|0\rangle,$$

we can rewrite the Schrödinger equation $\hat{H}_0|\Psi(\delta\mathbf{k})\rangle = E(\delta\mathbf{k})|\Psi(\delta\mathbf{k})\rangle$ in the first-quantized formalism as

$$H^{(\eta)}(\delta\mathbf{k})\Psi(\delta\mathbf{k}) = E(\delta\mathbf{k})\Psi(\delta\mathbf{k}), \tag{C5}$$

with the Hamiltonian matrix

$$H^{(\eta)}_0(\mathbf{K}_M+\delta\mathbf{k}) = \begin{pmatrix} 0 & \phi^{(\eta)}(\mathbf{K}_M+\delta\mathbf{k}) & \phi^{(\eta)}(\mathbf{K}_M-\mathbf{b}_{M2}+\mathbf{b}_{M1}+\delta\mathbf{k}) & \phi^{(\eta)}(\mathbf{K}_M-\mathbf{b}_{M2}+\delta\mathbf{k}) \\ \phi^{\dagger(\eta)}(\mathbf{K}_M+\delta\mathbf{k}) & \mathcal{H}^{(\eta)}(\mathbf{K}_M+\delta\mathbf{k}) & 0 & 0 \\ \phi^{\dagger(\eta)}(\mathbf{K}_M-\mathbf{b}_{M2}+\mathbf{b}_{M1}+\delta\mathbf{k}) & 0 & \mathcal{H}^{(\eta)}(\mathbf{K}_M-\mathbf{b}_{M2}+\mathbf{b}_{M1}+\delta\mathbf{k}) & 0 \\ \phi^{\dagger(\eta)}(\mathbf{K}_M-\mathbf{b}_{M2}+\delta\mathbf{k}) & 0 & 0 & \mathcal{H}^{(\eta)}(\mathbf{K}_M-\mathbf{b}_{M2}+\delta\mathbf{k}) \end{pmatrix} \tag{C6}$$

acting on the 14-dimensional spinor

$$\Psi(\delta\mathbf{k}) = \Big(\psi^{(f)}(\delta\mathbf{k}),\psi^{(0c)}(\delta\mathbf{k}),\psi^{(1c)}(\delta\mathbf{k}),\psi^{(2c)}(\delta\mathbf{k})\Big). \tag{C7}$$

Defining $\mathbf{G}_0 = \mathbf{0}$, $\mathbf{G}_1 = \mathbf{b}_{M2} - \mathbf{b}_{M1}$, and $\mathbf{G}_2 = \mathbf{b}_{M2}$, the component form of the first-quantized formalism is

$$\sum_{i=0,1,2}\phi^{(\eta)}(\mathbf{K}_M - \mathbf{G}_i + \delta\mathbf{k})\psi^{(ic)} = E\psi^{(f)}, \tag{C8}$$

$$\phi^{\dagger(\eta)}(\mathbf{K}_M-\mathbf{G}_i+\delta\mathbf{k})\psi^{(f)}+\mathcal{H}^{(\eta)}(\mathbf{K}_M-\mathbf{G}_i+\delta\mathbf{k})\psi^{(ic)}=E\psi^{(ic)},\quad i=0,1,2. \tag{C9}$$

Rearranging the second equation, we get $\psi^{(ic)}=(E-\mathcal{H}^{(\eta)}(\mathbf{K}_M-\mathbf{G}_i+\delta\mathbf{k}))^{-1}\phi^{\dagger(\eta)}(\mathbf{K}_M-\mathbf{G}_i+\delta\mathbf{k})\psi^{(f)}$ and inserting the expression into the first equation:

$$E\psi^{(f)}=\sum_{i=0,1,2}\phi^{(\eta)}(\mathbf{K}_M-\mathbf{G}_i+\delta\mathbf{k})\left(E-\mathcal{H}^{(\eta)}(\mathbf{K}_M-\mathbf{G}_i+\delta\mathbf{k})\right)^{-1}\phi^{\dagger(\eta)}(\mathbf{K}_M-\mathbf{G}_i+\delta\mathbf{k})\psi^{(f)}. \tag{C10}$$

The determinant of $(E-\mathcal{H}^{(\eta)}(\mathbf{k}))$ is

$$E^4-E^2(M^2+2v_\star^2k^2)+v_\star^4k^4. \tag{C11}$$

We neglect $\mathcal{O}(E^2)$ at K_M and $\bar{K}_M$ and, using the identity $\eta^2=+1$,

$$\left(E-\mathcal{H}^{(\eta)}(\mathbf{k})\right)^{-1}\approx \frac{1}{v_\star^4|\mathbf{k}|^4}\begin{pmatrix}(-M^2-v_\star^2|\mathbf{k}|^2)E\sigma_0-Mv_\star^2((k_y^2-k_x^2)\sigma_x+2k_xk_y\eta\sigma_y) & -v_\star^3|\mathbf{k}|^2(\eta k_x\sigma_0+ik_y\sigma_z)+Mv_\star E(\eta k_x\sigma_x-k_y\sigma_y)\\ -v_\star^3|\mathbf{k}|^2(\eta k_x\sigma_0-ik_y\sigma_z)+Mv_\star E(\eta k_x\sigma_x-k_y\sigma_y) & -v_\star^2|\mathbf{k}|^2E\sigma_0\end{pmatrix}. \tag{C12}$$

Using Eq. (C12) in Eq. (C10) and expanding to first order in $\delta\mathbf{k}$, where we also neglect the product of $\delta\mathbf{k}$ and E, Eq. (C10) reduces to

$$\begin{aligned}E\psi^{(f)}&=-\frac{3\gamma_K^2(M^2+D^2)(K_\theta^2a_\star^2+1)}{D^4}E\psi^{(f)}-\frac{3M\gamma_K^2(2(1+a_\star^2K_\theta^2)+\tilde{\lambda}^2(1-K_\theta a_\star)(K_\theta a_\star+1))}{K_\theta D^2}(\sigma_x\delta k_y-\sigma_y\delta k_x)\psi^{(f)}\\&\approx-\left(\frac{3\gamma_K^2(K_\theta^2a_\star^2+1)}{D^2}E+\left(\frac{3M}{D}\right)\left(\frac{\gamma_K}{D}\right)^2(2(1+a_\star^2K_\theta^2)+\tilde{\lambda}^2(1-K_\theta a_\star)(K_\theta a_\star+1))v_\star(\sigma_x\delta k_y-\sigma_y\delta k_x)\right)\psi^{(f)},\end{aligned} \tag{C13}$$

where the last line is obtained because $D\gg M$ and $\gamma_K=\gamma_0e^{-\tilde{\lambda}^2/2}$. We can identify a velocity $\tilde{v}_D$ and the Z factor from a self-energy treatment of the f electrons, where the Dirac velocity at the K_M points is

$$v_D=Z\tilde{v}_D. \tag{C14}$$

The velocity

$$\tilde{v}_D=3\left(\frac{M}{D}\right)\left(\frac{\gamma_K}{D}\right)^2(2(1+a_\star^2K_\theta^2)+\tilde{\lambda}^2(1-K_\theta a_\star)(K_\theta a_\star+1))v_\star, \tag{C15}$$

and the Z factor is

$$Z=\left(1+3\left(\frac{\gamma_K}{D}\right)^2(K_\theta^2a_\star^2+1)\right)^{-1}\approx 1 \tag{C16}$$

because $(\gamma_K/D)\ll 1$. Rearranging yields the final result

$$E\psi^{(f)}=-v_D(\sigma_x\delta k_y-\sigma_y\delta k_x)\psi^{(f)}, \tag{C17}$$

linearized near the K_M point and

$$v_D=3\left(\frac{M}{D}\right)\left(\frac{\gamma_K}{D}\right)^2(2(1+a_\star^2K_\theta^2)+\tilde{\lambda}^2(1-a_\star^2K_\theta^2))v_\star, \tag{C18}$$

corresponding to Eq. (22). Taking the $a_\star=0$ limit gives

$$v_D|_{a_\star=0}=3\left(\frac{M}{D}\right)\left(\frac{\gamma_K}{D}\right)^2(2+\tilde{\lambda}^2)v_\star. \tag{C19}$$

Repeating the calculation for the $\bar{K}_M$ point in the $\eta=+1$ valley results in $v_D(\sigma_x\delta k_y-\sigma_y\delta k_x)\psi^{(f)}=E\psi^{(f)}$, which has the same chirality as the Dirac cone at K_M in the same valley. The Dirac cone structure of the topological heavy-fermion model for the K'_M and $\bar{K}'_M$ points in the $\eta=-1$ valley is $-v_D(\sigma_x\delta k_y+\sigma_y\delta k_x)$ and $v_D(\sigma_x\delta k_y+\sigma_y\delta k_x)$. Note that the chirality of the Dirac cones in the $\eta=-1$ valley is opposite to the Dirac cones in the $\eta=+1$ valley.

APPENDIX D: DERIVATION OF THE CONDUCTION DENSITY OF STATES IN THE Γ_3 CHANNEL

Here, we derive the conduction electron density of states (26) in the Γ_3 channel which hybridizes with the localized f states. The conduction electron Hamiltonian has the form

$$\mathcal{H}^{(\eta)}(\mathbf{k}) = v_\star(\eta k_x \tau_1 \otimes \alpha_0 - k_y \tau_2 \otimes \alpha_z) + \frac{1}{2}M(1-\tau_z)\otimes\alpha_x = \begin{pmatrix} & v_\star \alpha_x(\vec{k}_\eta\cdot\vec{\alpha}) \\ v_\star(\vec{k}_\eta\cdot\vec{\alpha})\alpha_x & M\alpha_x \end{pmatrix}. \tag{D1}$$

Here, the upper left two-by-two block is the Γ_3 irreducible representation that hybridizes with the localized f states, and the lower two-by-two block is the $\Gamma_{1,2}$ irreducible representation that does not hybridize. The Pauli matrices $\alpha_\mu \equiv (\alpha_0, \vec{\alpha})$ $(\mu = 0,\ 3)$ act on the two-dimensional blocks, while the isospin matrices $(1, \vec{\tau})$ act on the two-dimensional blocks that define the space of representations, so that $P_{\Gamma_3} = \frac{1}{2}(1+\tau_z)$ projects into the Γ_3 channel. Here, we have adopted the notation $\vec{k}_\eta = (\eta k_x, k_y)$, so that $\vec{k}_\eta \cdot \vec{\alpha} = \eta k_x \alpha_x + k_y \alpha_y$. The conduction sea is particle-hole symmetric with energy eigenvalues given by $\pm E_\pm(\mathbf{k})$, where

$$E_\pm(\mathbf{k}) = \pm\frac{M}{2} + \sqrt{\left(\frac{M}{2}\right)^2 + (v_\star k)^2} \tag{D2}$$

and $k \equiv |\mathbf{k}|$. The particle-hole symmetry allows us to write the total conduction density of states as $\rho_{\mathrm{TOT}}(\omega) = \rho_+(\omega) + \rho_-(\omega)$, where

$$\rho_\pm(\omega) = \sum_{\mathbf{k}} \delta(\omega - |E_\pm(\mathbf{k})|) = \frac{(2\pi)^2}{A_K}\int \frac{2\pi k dk}{(2\pi)^2}\delta(\omega - |E_\pm(\mathbf{k})|) = \frac{\pi}{A_k}\int \frac{dk^2}{dE_\pm(\mathbf{k})} dE_\pm \delta(\omega - |E_\pm(\mathbf{k})|) = \frac{\pi}{A_k}\left(\frac{dk^2}{dE_\pm}|_{E_\pm = |\omega|}\theta(|\omega| \mp M)\right), \tag{D3}$$

where $A_k = 3\sqrt{3}/2K_\theta^2$ is the area of the hexagonal moiré Brillouin zone and θ is the Heaviside step function. By noting $dk^2/dE_\pm = (2E_\pm(\mathbf{k}) \mp M)/v_\star^2$, we get

$$\rho_\pm(\omega) = \frac{2\pi}{3\sqrt{3}}\frac{(2|\omega| \mp M)}{v_\star^2 K_\theta^2}\theta(|\omega| \mp M) \tag{D4}$$

as the c-electron density of states per spin per valley. Next, we project the conduction electron propagator into the Γ_3 channel by integrating out the $\Gamma_{1,2}$ electrons:

$$G_c^{\Gamma_3}(k,\omega) = P_{\Gamma_3}\frac{1}{[\omega - \mathcal{H}^{(\eta)}(\mathbf{k})]}P_{\Gamma_3} = \left(\omega - v_\star^2\alpha_x(\vec{k}_\eta\cdot\vec{\alpha})\frac{1}{\omega - M\alpha_x}(\vec{k}_\eta\cdot\vec{\alpha})\alpha_x\right)^{-1}. \tag{D5}$$

Simplifying, we obtain

$$G_c^{\Gamma_3}(k,\omega) = (\omega^2 - M^2)\frac{\omega[\omega^2 - M^2 - (v_\star k)^2] + Mv_\star^2[(k_x^2 - k_y^2)\alpha_x - (2\eta k_x k_y)\alpha_y]}{[\omega(\omega^2 - M^2 - (v_\star k)^2)]^2 - (Mv_\star^2 k^2)^2} = (\omega^2 - M^2)\frac{\omega[\omega^2 - M^2 - (v_\star k)^2] + Mv_\star^2[(k_x^2 - k_y^2)\alpha_x - (2\eta k_x k_y)\alpha_y]}{(\omega^2 - M^2)(\omega^2 - E_+(\mathbf{k})^2)(\omega^2 - E_-(\mathbf{k})^2)}. \tag{D6}$$

The trace of Eq. (D6) resolved along its poles gives

$$\mathrm{Tr}G_c^{\Gamma_3}(k,\omega) = 2\frac{\omega[\omega^2 - M^2 - (v_\star k)^2]}{(\omega^2 - E_+^2(\mathbf{k}))(\omega^2 - E_-^2(\mathbf{k}))} = \left\{\frac{E_-(\mathbf{k}) + M}{2E_-(\mathbf{k}) + M}\left(\frac{1}{\omega - E_-(\mathbf{k})} + \frac{1}{\omega + E_-(\mathbf{k})}\right) + \frac{E_+(\mathbf{k}) - M}{2E_+(\mathbf{k}) - M}\left(\frac{1}{\omega - E_+(\mathbf{k})} + \frac{1}{\omega + E_+(\mathbf{k})}\right)\right\}. \tag{D7}$$

The conduction c-electron density of states, per spin per valley and per orbital in the Γ_3 channel that hybridizes with the localized f states, is defined as the following:

$$\rho_c^{\Gamma_3}(\omega) = \frac{1}{2\pi}\sum_{\mathbf{k}} \mathrm{Im}\,\mathrm{Tr} G_c^{\Gamma_3}(k,\omega - i\delta) = \frac{1}{2}\sum_{\mathbf{k}}\left\{\frac{E_-(\mathbf{k})+M}{2E_-(\mathbf{k})+M}\delta[\omega - |E_-(\mathbf{k})|] + \frac{E_+(\mathbf{k})-M}{2E_+(\mathbf{k})-M}\delta[|\omega| - |E_+(\mathbf{k})|]\right\}$$
$$= \frac{1}{2}\left\{\frac{|\omega|+M}{2|\omega|+M}\rho_-(\omega) + \frac{|\omega|-M}{2|\omega|-M}\rho_+(\omega)\right\}, \tag{D8}$$

where the factor of a half is to account for the valley degeneracy. Recalling $\rho_\pm(\omega)$ from Eq. (D4), our final expression for the conduction c-electron density of states per spin per valley and per orbital in the Γ_3 channel is

$$\rho_c^{\Gamma_3}(\omega) = \frac{A}{D^2}\left(\frac{1}{2}(|\omega|+M)\theta(M-|\omega|) + \frac{1}{2}|\omega|\theta(|\omega|-M)\right) = \frac{A}{D^2}\times\begin{cases}|E|, & |E|>M,\\ \frac{1}{2}(|E|+M), & |E|<M,\end{cases} \tag{D9}$$

where $A = 2\pi/(3\sqrt{3})$ and $D = v_\star K_\theta$. In the main body of the text (26), we drop the Γ_3 superscript for clarity.

APPENDIX E: VARIANCE OF THE HYBRIDIZATION

Here, we evaluate the variance or mean square of the hybridization referred to in Eq. (27). We recall the hybridization matrix (9):

$$\phi^{(\eta)}(\mathbf{k}) \equiv \phi^{(\eta)}(\mathbf{k},\gamma_0) = e^{-|\mathbf{k}|^2\lambda^2/2}\Big(\alpha_0 + a_\star(\eta k_x\alpha_x + k_y\alpha_y),\ 0_{2\times 2}\Big). \tag{E1}$$

The square of the hybridization matrix (9) is then

$$\gamma_0^2\phi^{(\eta)}(\mathbf{k})\phi^{\dagger(\eta)}(\mathbf{k}) = \gamma_0^2 e^{-|\mathbf{k}|^2\lambda^2}(1 + a_\star^2(k_x^2+k_y^2)\alpha_0 - 2a_\star(\eta k_x\alpha_x + k_y\alpha_y)), \tag{E2}$$

where the Pauli matrices $\alpha_\mu \equiv (\alpha_0, \vec{\alpha})$ ($\mu = 0, 3$) act on the two-dimensional blocks. The off-diagonal terms of Eq. (E2) average to zero when we take a momentum integrated average over a circle of radius K_θ because they are odd in k_x and k_y. Averaging only the diagonal part of Eq. (E2) over a circle of radius K_θ yields

$$\overline{\gamma_0^2\phi^{(\eta)}(\mathbf{k})\phi^{\dagger(\eta)}(\mathbf{k})} = \frac{\gamma_0^2}{\pi K_\theta^2}\int_0^{2\pi}\int_0^{K_\theta} e^{-k^2\lambda^2}(1+a_\star^2k^2)\alpha_0 dk d\theta = \gamma_0^2\left[\frac{a_\star^2+\lambda^2 - e^{-\tilde{\lambda}^2}(\lambda^2 + a_\star^2(1+\tilde{\lambda}^2))}{\lambda^2\tilde{\lambda}^2}\right]\alpha_0 \equiv \overline{\gamma_0^2(k)}\alpha_0. \tag{E3}$$

Using the approximate scales for the parameters in the SB model [24,68] $\gamma_0 = 25\,\mathrm{meV}$, $M = 3.7\,\mathrm{meV}$, $v_\star = -4.3\,\mathrm{eV\,Å}$, $K_\theta = 0.031$ Å^{-1}, $a_\star = 65$ Å, and $\lambda = 0.225 a_M = 29$ Å for the size of the Wannier states, which gives $\tilde{\lambda} = \lambda K_\theta = 0.90$, we calculate the momentum integrated average of the hybridization over a circle of radius K_θ to be

$$\overline{\gamma_0^2(k)} = 1.891\gamma_0^2 \approx 2\gamma_0^2 = 1250\ (\mathrm{meV})^2, \tag{E4}$$

where the last equality follows from taking the bare hybridization $\gamma_0 = 25$ meV.

[1] G. Li, A. Luican, J. M. B. Lopes dos Santos, A. H. Castro Neto, A. Reina, J. Kong, and E. Y. Andrei, *Observation of van Hove singularities in twisted graphene layers*, Nat. Phys. **6**, 109 (2010).

[2] R. Bistritzer and A. H. MacDonald, *Moire bands in twisted double-layer graphene*, Proc. Natl. Acad. Sci. U.S.A. **108**, 12233 (2011).

[3] Y. Cao, V. Fatemi, S. Fang, K. Watanabe, T. Taniguchi, E. Kaxiras, and P. Jarillo-Herrero, *Unconventional superconductivity in magic-angle graphene superlattices*, Nature (London) **556**, 43 (2018).

[4] Y. Cao, V. Fatemi, A. Demir, S. Fang, S. L. Tomarken, J. Y. Luo, J. D. Sanchez-Yamagishi, K. Watanabe, T. Taniguchi, E. Kaxiras, R. C. Ashoori, and P. Jarillo-Herrero, *Correlated insulator behaviour at half-filling in magic-angle graphene superlattices*, Nature (London) **556**, 80 (2018).

[5] E. Y. Andrei and A. H. MacDonald, *Graphene bilayers with a twist*, Nat. Mater. **19**, 1265 (2020).

[6] E. Y. Andrei, D. K. Efetov, P. Jarillo-Herrero, A. H. MacDonald, K. F. Mak, T. Senthil, E. Tutuc, A. Yazdani, and A. F. Young, *The marvels of moiré materials*, Nat. Rev. Mater. **6**, 201 (2021).

[7] B. Lian, Z.-D. Song, N. Regnault, D. K. Efetov, A. Yazdani, and B. A. Bernevig, *Twisted bilayer graphene. IV. Exact insulator ground states and phase diagram*, Phys. Rev. B **103**, 205414 (2021).

[8] J. Liu, Z. Ma, J. Gao, and X. Dai, *Quantum valley Hall effect, orbital magnetism, and anomalous Hall effect in twisted multilayer graphene systems*, Phys. Rev. X **9**, 031021 (2019).

[9] C. Repellin, Z. Dong, Y.-H. Zhang, and T. Senthil, *Ferromagnetism in narrow bands of moiré superlattices*, Phys. Rev. Lett. **124**, 187601 (2020).

[10] F. Wu and S. Das Sarma, *Collective excitations of quantum anomalous Hall ferromagnets in twisted bilayer graphene*, Phys. Rev. Lett. **124**, 046403 (2020).
[11] J. H. Pixley and E. Y. Andrei, *Ferromagnetism in magic-angle graphene*, Science **365**, 543 (2019).
[12] Y. Cao, D. Chowdhury, D. Rodan-Legrain, O. Rubies-Bigorda, K. Watanabe, T. Taniguchi, T. Senthil, and P. Jarillo-Herrero, *Strange metal in magic-angle graphene with near Planckian dissipation*, Phys. Rev. Lett. **124**, 076801 (2020).
[13] R. Lyu, Z. Tuchfeld, N. Verma, H. Tian, K. Watanabe, T. Taniguchi, C. N. Lau, M. Randeria, and M. Bockrath, *Strange metal behavior of the Hall angle in twisted bilayer graphene*, Phys. Rev. B **103**, 245424 (2021).
[14] S. Das Sarma and F. Wu, *Strange metallicity of moiré twisted bilayer graphene*, Phys. Rev. Res. **4**, 033061 (2022).
[15] P. Cha, A. A. Patel, and E.-A. Kim, *Strange metals from melting correlated insulators in twisted bilayer graphene*, Phys. Rev. Lett. **127**, 266601 (2021).
[16] B. Ghawri, P. S. Mahapatra, M. Garg, S. Mandal, S. Bhowmik, A. Jayaraman, R. Soni, K. Watanabe, T. Taniguchi, H. R. Krishnamurthy, M. Jain, S. Banerjee, U. Chandni, and A. Ghosh, *Breakdown of semiclassical description of thermoelectricity in near-magic angle twisted bilayer graphene*, Nat. Commun. **13**, 1522 (2022).
[17] H. S. Arora, R. Polski, Y. Zhang, A. Thomson, Y. Choi, H. Kim, Z. Lin, I. Z. Wilson, X. Xu, J.-H. Chu, K. Watanabe, T. Taniguchi, J. Alicea, and S. Nadj-Perge, *Superconductivity in metallic twisted bilayer graphene stabilized by* WSe_2, Nature (London) **583**, 379 (2020).
[18] H. Polshyn, M. Yankowitz, S. Chen, Y. Zhang, K. Watanabe, T. Taniguchi, C. R. Dean, and A. F. Young, *Large linear-in-temperature resistivity in twisted bilayer graphene*, Nat. Phys. **15**, 1011 (2019).
[19] A. Jaoui, I. Das, G. Di Battista, J. Díez-Mérida, X. Lu, K. Watanabe, T. Taniguchi, H. Ishizuka, L. Levitov, and D. K. Efetov, *Quantum critical behaviour in magic-angle twisted bilayer graphene*, Nat. Phys. **18**, 633 (2022).
[20] E. Codecido, Q. Wang, R. Koester, S. Che, H. Tian, R. Lv, S. Tran, K. Watanabe, T. Taniguchi, F. Zhang, M. Bockrath, and C. N. Lau, *Correlated insulating and superconducting states in twisted bilayer graphene below the magic angle*, Sci. Adv. **5**, eaaw9770 (2019).
[21] M. Yankowitz, S. Chen, H. Polshyn, Y. Zhang, K. Watanabe, T. Taniguchi, D. Graf, A. F. Young, and C. R. Dean, *Tuning superconductivity in twisted bilayer graphene*, Science **363**, 1059 (2019).
[22] A. Ramires and J. L. Lado, *Electrically tunable gauge fields in tiny-angle twisted bilayer graphene*, Phys. Rev. Lett. **121**, 146801 (2018).
[23] M. Haule, E. Y. Andrei, and K. Haule, *The Mott-semiconducting state in the magic angle bilayer graphene*, arXiv:1901.09852.
[24] Z.-D. Song and B. A. Bernevig, *MATBG as topological heavy fermion: I. Exact mapping and correlated insulators*, Phys. Rev. Lett. **129**, 047601 (2022).
[25] H. Shi and X. Dai, *Heavy fermion representation for twisted bilayer graphene systems*, Phys. Rev. B **106**, 245129 (2022).
[26] N. Bultinck, E. Khalaf, S. Liu, S. Chatterjee, A. Vishwanath, and M. P. Zaletel, *Ground state and hidden symmetry of magic-angle graphene at even integer filling*, Phys. Rev. X **10**, 031034 (2020).
[27] M. Xie and A. H. MacDonald, *Nature of the correlated insulator states in twisted bilayer graphene*, Phys. Rev. Lett. **124**, 097601 (2020).
[28] Y. Zhang, K. Jiang, Z. Wang, and F. Zhang, *Correlated insulating phases of twisted bilayer graphene at commensurate filling fractions: A Hartree-Fock study*, Phys. Rev. B **102**, 035136 (2020).
[29] L. Balents, C. R. Dean, D. K. Efetov, and A. F. Young, *Superconductivity and strong correlations in moiré flat bands*, Nat. Phys. **16**, 725 (2020).
[30] B. Lian, Z. Wang, and B. A. Bernevig, *Twisted bilayer graphene: A phonon-driven superconductor*, Phys. Rev. Lett. **122**, 257002 (2019).
[31] S. Liu, E. Khalaf, J. Y. Lee, and A. Vishwanath, *Nematic topological semimetal and insulator in magic-angle bilayer graphene at charge neutrality*, Phys. Rev. Res. **3**, 013033 (2021).
[32] C.-C. Liu, L.-D. Zhang, W.-Q. Chen, and F. Yang, *Chiral spin density wave and* $d+id$ *superconductivity in the magic-angle-twisted bilayer graphene*, Phys. Rev. Lett. **121**, 217001 (2018).
[33] F. Wu, A. H. MacDonald, and I. Martin, *Theory of phonon-mediated superconductivity in twisted bilayer graphene*, Phys. Rev. Lett. **121**, 257001 (2018).
[34] F. Xie, Z. Song, B. Lian, and B. A. Bernevig, *Topology-bounded superfluid weight in twisted bilayer graphene*, Phys. Rev. Lett. **124**, 167002 (2020).
[35] C. Xu and L. Balents, *Topological superconductivity in twisted multilayer graphene*, Phys. Rev. Lett. **121**, 087001 (2018).
[36] C. Lewandowski, D. Chowdhury, and J. Ruhman, *Pairing in magic-angle twisted bilayer graphene: Role of phonon and plasmon umklapp*, Phys. Rev. B **103**, 235401 (2021).
[37] P. J. Ledwith, G. Tarnopolsky, E. Khalaf, and A. Vishwanath, *Fractional Chern insulator states in twisted bilayer graphene: An analytical approach*, Phys. Rev. Res. **2**, 023237 (2020).
[38] E. Khalaf, S. Chatterjee, N. Bultinck, M. P. Zaletel, and A. Vishwanath, *Charged skyrmions and topological origin of superconductivity in magic-angle graphene*, Sci. Adv. **7**, eabf5299 (2021).
[39] E. J. König, P. Coleman, and A. M. Tsvelik, *Spin magnetometry as a probe of stripe superconductivity in twisted bilayer graphene*, Phys. Rev. B **102**, 104514 (2020).
[40] D. V. Chichinadze, L. Classen, and A. V. Chubukov, *Nematic superconductivity in twisted bilayer graphene*, Phys. Rev. B **101**, 224513 (2020).
[41] J. González and T. Stauber, *Kohn-Luttinger superconductivity in twisted bilayer graphene*, Phys. Rev. Lett. **122**, 026801 (2019).
[42] F. Guinea and N. R. Walet, *Electrostatic effects, band distortions, and superconductivity in twisted graphene bilayers*, Proc. Natl. Acad. Sci. U.S.A. **115**, 13174 (2018).
[43] T. Huang, L. Zhang, and T. Ma, *Antiferromagnetically ordered Mott insulator and* $\mathrm{d}+\mathrm{id}$ *superconductivity in*

twisted bilayer graphene: A quantum Monte Carlo study, Sci. Bull. **64**, 310 (2019).

[44] H. Isobe, N. F. Q. Yuan, and L. Fu, *Unconventional superconductivity and density waves in twisted bilayer graphene*, Phys. Rev. X **8**, 041041 (2018).

[45] A. Julku, T. J. Peltonen, L. Liang, T. T. Heikkilä, and P. Törmä, *Superfluid weight and Berezinskii-Kosterlitz-Thouless transition temperature of twisted bilayer graphene*, Phys. Rev. B **101**, 060505(R) (2020).

[46] D. M. Kennes, J. Lischner, and C. Karrasch, *Strong correlations and $d+id$ superconductivity in twisted bilayer graphene*, Phys. Rev. B **98**, 241407(R) (2018).

[47] A. Datta, M. J. Calderón, A. Camjayi, and E. Bascones, *Heavy quasiparticles and cascades without symmetry breaking in twisted bilayer graphene*, Nat. Commun. **14**, 5036 (2023).

[48] K. Zhang, Y. Zhang, L. Fu, and E.-A. Kim, *Fractional correlated insulating states at one-third filled magic angle twisted bilayer graphene*, Commun. Phys. **5**, 250 (2022).

[49] D. Mao, K. Zhang, and E.-A. Kim, *Fractionalization in fractional correlated insulating states at $n \pm 1/3$ filled twisted bilayer graphene*, Phys. Rev. Lett. **131**, 106801 (2023).

[50] D. Wong, K. P. Nuckolls, M. Oh, B. Lian, Y. Xie, S. Jeon, K. Watanabe, T. Taniguchi, B. A. Bernevig, and A. Yazdani, *Cascade of electronic transitions in magic-angle twisted bilayer graphene*, Nature (London) **582**, 198 (2020).

[51] U. Zondiner, A. Rozen, D. Rodan-Legrain, Y. Cao, R. Queiroz, T. Taniguchi, K. Watanabe, Y. Oreg, F. von Oppen, A. Stern, E. Berg, P. Jarillo-Herrero, and S. Ilani, *Cascade of phase transitions and Dirac revivals in magic-angle graphene*, Nature (London) **582**, 203 (2020).

[52] Y. Saito, F. Yang, J. Ge, X. Liu, T. Taniguchi, K. Watanabe, J. I. A. Li, E. Berg, and A. F. Young, *Isospin Pomeranchuk effect in twisted bilayer graphene*, Nature (London) **592**, 220 (2021).

[53] X. Lu, P. Stepanov, W. Yang, M. Xie, M. A. Aamir, I. Das, C. Urgell, K. Watanabe, T. Taniguchi, G. Zhang, A. Bachtold, A. H. MacDonald, and D. K. Efetov, *Superconductors, orbital magnets and correlated states in magic-angle bilayer graphene*, Nature (London) **574**, 653 (2019).

[54] A. Rozen, J. M. Park, U. Zondiner, Y. Cao, D. Rodan-Legrain, T. Taniguchi, K. Watanabe, Y. Oreg, A. Stern, E. Berg, P. Jarillo-Herrero, and S. Ilani, *Entropic evidence for a Pomeranchuk effect in magic-angle graphene*, Nature (London) **592**, 214 (2021).

[55] Y. Xie, B. Lian, B. Jäck, X. Liu, C.-L. Chiu, K. Watanabe, T. Taniguchi, B. A. Bernevig, and A. Yazdani, *Spectroscopic signatures of many-body correlations in magic-angle twisted bilayer graphene*, Nature (London) **572**, 101 (2019).

[56] Z. Song, Z. Wang, W. Shi, G. Li, C. Fang, and B. A. Bernevig, *All magic angles in twisted bilayer graphene are topological*, Phys. Rev. Lett. **123**, 036401 (2019).

[57] L. Zou, H. C. Po, A. Vishwanath, and T. Senthil, *Band structure of twisted bilayer graphene: Emergent symmetries, commensurate approximants, and Wannier obstructions*, Phys. Rev. B **98**, 085435 (2018).

[58] D. K. Efimkin and A. H. MacDonald, *Helical network model for twisted bilayer graphene*, Phys. Rev. B **98**, 035404 (2018).

[59] K. P. Nuckolls, M. Oh, D. Wong, B. Lian, K. Watanabe, T. Taniguchi, B. A. Bernevig, and A. Yazdani, *Strongly correlated Chern insulators in magic-angle twisted bilayer graphene*, Nature (London) **588**, 610 (2020).

[60] A. T. Pierce, Y. Xie, J. M. Park, E. Khalaf, S. H. Lee, Y. Cao, D. E. Parker, P. R. Forrester, S. Chen, K. Watanabe, T. Taniguchi, A. Vishwanath, P. Jarillo-Herrero, and A. Yacoby, *Unconventional sequence of correlated Chern insulators in magic-angle twisted bilayer graphene*, Nat. Phys. **17**, 1210 (2021).

[61] K. Hejazi, X. Chen, and L. Balents, *Hybrid Wannier Chern bands in magic angle twisted bilayer graphene and the quantized anomalous Hall effect*, Phys. Rev. Res. **3**, 013242 (2021).

[62] Y. Saito, J. Ge, L. Rademaker, K. Watanabe, T. Taniguchi, D. A. Abanin, and A. F. Young, *Hofstadter subband ferromagnetism and symmetry-broken Chern insulators in twisted bilayer graphene*, Nat. Phys. **17**, 478 (2021).

[63] Y. Choi, H. Kim, Y. Peng, A. Thomson, C. Lewandowski, R. Polski, Y. Zhang, H. S. Arora, K. Watanabe, T. Taniguchi, J. Alicea, and S. Nadj-Perge, *Correlation-driven topological phases in magic-angle twisted bilayer graphene*, Nature (London) **589**, 536 (2021).

[64] S. Wu, Z. Zhang, K. Watanabe, T. Taniguchi, and E. Y. Andrei, *Chern insulators, van Hove singularities and topological flat bands in magic-angle twisted bilayer graphene*, Nat. Mater. **20**, 488 (2021).

[65] J. Kang and O. Vafek, *Non-Abelian Dirac node braiding and near-degeneracy of correlated phases at odd integer filling in magic-angle twisted bilayer graphene*, Phys. Rev. B **102**, 035161 (2020).

[66] H. C. Po, L. Zou, T. Senthil, and A. Vishwanath, *Faithful tight-binding models and fragile topology of magic-angle bilayer graphene*, Phys. Rev. B **99**, 195455 (2019).

[67] B. Lian, F. Xie, and B. A. Bernevig, *Landau level of fragile topology*, Phys. Rev. B **102**, 041402(R) (2020).

[68] D. Călugăru, M. Borovkov, L. L. H. Lau, P. Coleman, Z.-D. Song, and B. A. Bernevig, *Twisted bilayer graphene as topological heavy fermion: II. Analytical approximations of the model parameters*, Fiz. Nizk. Temp. **49**, 703 (2023).

[69] Y.-Z. Chou and S. Das Sarma, *Kondo lattice model in magic-angle twisted bilayer graphene*, Phys. Rev. Lett. **131**, 026501 (2023).

[70] H. Hu, B. A. Bernevig, and A. M. Tsvelik, *Kondo lattice model of magic-angle twisted-bilayer graphene: Hund's rule, local-moment fluctuations, and low-energy effective theory*, Phys. Rev. Lett. **131**, 026502 (2023).

[71] H. Hu, G. Rai, L. Crippa, J. Herzog-Arbeitman, D. Călugăru, T. Wehling, G. Sangiovanni, R. Valentí, A. M. Tsvelik, and B. A. Bernevig, *Symmetric Kondo lattice states in doped strained twisted bilayer graphene*, Phys. Rev. Lett. **131**, 166501 (2023).

[72] Y. Li, B. M. Fregoso, and M. Dzero, *Topological mixed valence model in magic-angle twisted bilayer graphene*, Phys. Rev. B **110**, 045123 (2024).

[73] G.-D. Zhou, Y.-J. Wang, N. Tong, and Z.-D. Song, *Kondo phase in twisted bilayer graphene*, Phys. Rev. B **109**, 045419 (2024).
[74] G. Rai, L. Crippa, D. Călugăru, H. Hu, F. Paoletti, L. de' Medici, A. Georges, B. A. Bernevig, R. Valentí, G. Sangiovanni, and T. Wehling, *Dynamical correlations and order in magic-angle twisted bilayer graphene*, Phys. Rev. X **14**, 031045 (2024).
[75] S. Florens and A. Georges, *Quantum impurity solvers using a slave rotor representation*, Phys. Rev. B **66**, 165111 (2002).
[76] S. Florens and A. Georges, *Slave-rotor mean-field theories of strongly correlated systems and the Mott transition in finite dimensions*, Phys. Rev. B **70**, 035114 (2004).
[77] A. C. Hewson, *The Kondo Problem to Heavy Fermions* (Cambridge University Press, Cambridge, England, 1993).
[78] J. Kondo, *Resistance minimum in dilute magnetic alloys*, Prog. Theor. Phys. **32**, 37 (1964).
[79] J. Kondo, *Anomalous Hall effect and magnetoresistance of ferromagnetic metals*, Prog. Theor. Phys. **27**, 772 (1962).
[80] P. Coleman, *Heavy fermions: Electrons at the edge of magnetism*, Handb. Magn. Adv. Magn. Mater. **1**, 95 (2007).
[81] Q. Si and F. Steglich, *Heavy fermions and quantum phase transitions*, Science **329**, 1161 (2010).
[82] S. Wirth and F. Steglich, *Exploring heavy fermions from macroscopic to microscopic length scales*, Nat. Rev. Mater. **1**, 1 (2016).
[83] G. R. Stewart, *Heavy-fermion systems*, Rev. Mod. Phys. **56**, 755 (1984).
[84] M. Dzero, K. Sun, V. Galitski, and P. Coleman, *Topological Kondo insulators*, Phys. Rev. Lett. **104**, 106408 (2010).
[85] D. Sherrington and P. Riseborough, *Ionic size effects in valence transitions*, J. Phys. (Paris), Colloq. **37**, C4-255 (1976).
[86] P. S. Riseborough, *Strong electron phonon interactions in mixed valent states*, J. Appl. Phys. **61**, 3171 (1987).
[87] C. Chen *et al.*, *Strong inter-valley electron-phonon coupling in magic-angle twisted bilayer graphene*, Nature (London) **636**, 342 (2024).
[88] L. Fritz and M. Vojta, *The physics of Kondo impurities in graphene*, Rep. Prog. Phys. **76**, 032501 (2013).
[89] D. Withoff and E. Fradkin, *Phase transitions in gapless Fermi systems with magnetic impurities*, Phys. Rev. Lett. **64**, 1835 (1990).
[90] D. E. Parker, T. Soejima, J. Hauschild, M. P. Zaletel, and N. Bultinck, *Strain-induced quantum phase transitions in magic-angle graphene*, Phys. Rev. Lett. **127**, 027601 (2021).
[91] Y. H. Kwan, G. Wagner, T. Soejima, M. P. Zaletel, S. H. Simon, S. A. Parameswaran, and N. Bultinck, *Kekulé spiral order at all nonzero integer fillings in twisted bilayer graphene*, Phys. Rev. X **11**, 041063 (2021).
[92] G. Wagner, Y. H. Kwan, N. Bultinck, S. H. Simon, and S. A. Parameswaran, *Global phase diagram of the normal state of twisted bilayer graphene*, Phys. Rev. Lett. **128**, 156401 (2022).
[93] K. P. Nuckolls, R. L. Lee, M. Oh, D. Wong, T. Soejima, J. P. Hong, D. Călugăru, J. Herzog-Arbeitman, B. A. Bernevig, K. Watanabe, T. Taniguchi, N. Regnault, M. P. Zaletel, and A. Yazdani, *Quantum textures of the many-body wavefunctions in magic-angle graphene*, Nature (London) **620**, 525 (2023).
[94] J. Herzog-Arbeitman, J. Yu, D. Călugăru, H. Hu, N. Regnault, O. Vafek, J. Kang, and B. A. Bernevig, *Heavy fermions as an efficient representation of atomistic strain and relaxation in twisted bilayer graphene*, arXiv:2405.13880.
[95] Y.-H. Zhang, D. Mao, and T. Senthil, *Twisted bilayer graphene aligned with hexagonal boron nitride: Anomalous Hall effect and a lattice model*, Phys. Rev. Res. **1**, 033126 (2019).
[96] D. Kaplan, T. Holder, and B. Yan, *Twisted photovoltaics at terahertz frequencies from momentum shift current*, Phys. Rev. Res. **4**, 013209 (2022).
[97] G. Tarnopolsky, A. J. Kruchkov, and A. Vishwanath, *Origin of magic angles in twisted bilayer graphene*, Phys. Rev. Lett. **122**, 106405 (2019).
[98] J. Wang, Y. Zheng, A. J. Millis, and J. Cano, *Chiral approximation to twisted bilayer graphene: Exact intravalley inversion symmetry, nodal structure, and implications for higher magic angles*, Phys. Rev. Res. **3**, 023155 (2021).
[99] A. Laturia, M. L. V. d. Put, and W. G. Vandenberghe, *Dielectric properties of hexagonal boron nitride and transition metal dichalcogenides: From monolayer to bulk*, npj 2D Mater. Appl. **2**, 6 (2018).
[100] D. Wong, K. P. Nuckolls, M. Oh, B. Lian, Y. Xie, S. Jeon, K. Watanabe, T. Taniguchi, B. A. Bernevig, and A. Yazdani, *Personal communication with the authors of Cascade of electronic transitions in magic-angle twisted bilayer graphene*, Nature (London) **582**, 198 (2020).
[101] J. R. Schrieffer and P. Wolff, *Relation between the Anderson and Kondo Hamiltonians*, Phys. Rev. **149**, 491 (1966).
[102] B. Coqblin and J. R. Schrieffer, *Exchange interaction in alloys with cerium impurities*, Phys. Rev. **185**, 847 (1969).
[103] We note that one of the weaknesses of the auxiliary boson approach in its current form is that the effective cutoff is given by the conduction bandwidth, about $2v_\star K_\theta = 2D$ rather than U as in Eq. (36) giving an artificially enhanced $T_K^{(1)}$, which we are adjusting for by reducing the effective Kondo coupling constant by adjusting the value of γ_0. A more realistic approach, to be explored in future work, will adopt a cutoff in the Matsubara sums $|\omega_n| < U$ associated with the electronic free energy in Eq. (57), which we believe will eliminate the need to make an adjustment in γ_0.
[104] R. Flint, M. Dzero, and P. Coleman, *Heavy electrons and the symplectic symmetry of spin*, Nat. Phys. **4**, 643 (2008).
[105] M. Maltseva, M. Dzero, and P. Coleman, *Electron cotunneling into a Kondo lattice*, Phys. Rev. Lett. **103**, 206402 (2009).
[106] H. Kobayashi, Y. Sakaguchi, H. Kitagawa, M. Oura, S. Ikeda, K. Kuga, S. Suzuki, S. Nakatsuji, R. Masuda, Y. Kobayashi, M. Seto, Y. Yoda, K. Tamasaku, Y. Komijani, P. Chandra, and P. Coleman, *Observation of a critical charge mode in a strange metal*, Science **379**, 908 (2023).

[107] M. Angeli, E. Tosatti, and M. Fabrizio, *Valley Jahn-Teller effect in twisted bilayer graphene*, Phys. Rev. X **9**, 041010 (2019).

[108] M. Angeli and M. Fabrizio, *Jahn-Teller coupling to moiré phonons in the continuum model formalism for small-angle twisted bilayer graphene*, Eur. Phys. J. Plus **135**, 630 (2020).

[109] C.-X. Liu, Y. Chen, A. Yazdani, and B. A. Bernevig, *Electron-k-phonon interaction in twisted bilayer graphene*, Phys. Rev. B **110**, 045133 (2024).

[110] H. Shi, W. Miao, and X. Dai, *Moiré optical phonons dancing with heavy electrons in magic-angle twisted bilayer graphene*, arXiv:2402.11824.

[111] Y.-J. Wang, G.-D. Zhou, S.-Y. Peng, B. Lian, and Z.-D. Song, *Molecular pairing in twisted bilayer graphene superconductivity*, Phys. Rev. Lett. **133**, 146001 (2024).

[112] Z. Zhu and T. P. Devereaux, *Microscopic theory for electron-phonon coupling in twisted bilayer graphene*, arXiv:2407.03293.

[113] J. Kang, B. A. Bernevig, and O. Vafek, *Cascades between light and heavy fermions in the normal state of magic-angle twisted bilayer graphene*, Phys. Rev. Lett. **127**, 266402 (2021).

[114] C. M. Varma, P. B. Littlewood, S. Schmitt-Rink, E. Abrahams, and A. E. Ruckenstein, *Phenomenology of the normal state of* $Cu-O$ *high-temperature superconductors*, Phys. Rev. Lett. **63**, 1996 (1989).

[115] F. Wu, E. Hwang, and S. Das Sarma, *Phonon-induced giant linear-in-t resistivity in magic angle twisted bilayer graphene: Ordinary strangeness and exotic superconductivity*, Phys. Rev. B **99**, 165112 (2019).